High-frequency asymptotic compression of dense BEM matrices

Daan Huybrechs
Peter Opsomer

Report TW 669, August 2016

KU Leuven
Department of Computer Science
Celestijnenlaan 200A – B-3001 Heverlee (Belgium)

High-frequency asymptotic compression of dense BEM matrices

Daan Huybrechs
Peter Opsomer

Report TW 669, August 2016

Department of Computer Science, KU Leuven

Abstract

High-frequency scattering problems in acoustics are often solved with boundary element methods. They lead to a discretization matrix that is typically large and dense, with the elements representing interactions between all parts of a scattering obstacle. However, the matrix represents the action of an oscillatory integral operator on an oscillatory density function, and at high frequencies this action is highly localized in nature. Asymptotic methods for high-frequency problems are based on extracting the phase of the density function via ray tracing or similar techniques. This results in a much smaller matrix, but this approach is very expensive for scattering obstacles with complex geometries. In this paper, we explore methods to exploit the asymptotic localization of the operator directly. We introduce sparsity in the original discretization matrix by modifying the Green's function with well-chosen smooth window functions. A relatively simple technique automatically decides where to place these windows for general geometries, thus providing valuable asymptotic information. We illustrate that such asymptotic compression can be achieved even for near-trapping domains and multiple scattering obstacles. Furthermore, we show robustness of the technique even for low-order BEM discretizations using piecewise linears or cubics in 2D, and preliminary results for 3D problems are encouraging. The cost of a matrix-vector product with respect to a full matrix is decreased after asymptotic compression, and in addition it appears that the condition number of the sparser matrix is much improved as well. On the other hand, we do not decrease the total number of degrees of freedom compared to a conventional discretization.

Keywords : Boundary Element Method, Oscillatory integration, High-frequency scattering, Compression, Condition number, Smooth window functions.
MSC : Primary : 65N38, Secondary : 65F50, 45A05, 45M05, 65R20

High-frequency asymptotic compression of dense BEM matrices

Daan Huybrechs*
Department of Computer Science
KU Leuven, Belgium

Peter Opsomer†
Department of Computer Science
KU Leuven, Belgium

August 4, 2016

Abstract

High-frequency scattering problems in acoustics are often solved with boundary element methods. They lead to a discretization matrix that is typically large and dense, with the elements representing interactions between all parts of a scattering obstacle. However, the matrix represents the action of an oscillatory integral operator on an oscillatory density function, and at high frequencies this action is highly localized in nature. Asymptotic methods for high-frequency problems are based on extracting the phase of the density function via ray tracing or similar techniques. This results in a much smaller matrix, but this approach is very expensive for scattering obstacles with complex geometries. In this paper, we explore methods to exploit the asymptotic localization of the operator directly. We introduce sparsity in the original discretization matrix by modifying the Green's function with well-chosen smooth window functions. A relatively simple technique automatically decides where to place these windows for general geometries, thus providing valuable asymptotic information. We illustrate that such asymptotic compression can be achieved even for near-trapping domains and multiple scattering obstacles. Furthermore, we show robustness of the technique even for low-order BEM discretizations using piecewise linears or cubics in 2D, and preliminary results for 3D problems are encouraging. The cost of a matrix-vector product with respect to a full matrix is decreased after asymptotic compression, and in addition it appears that the condition number of the sparser matrix is much improved as well. On the other hand, we do not decrease the total number of degrees of freedom compared to a conventional discretization.

1 Introduction

Numerical simulations in acoustics are often based on a Boundary Integral equation reformulation of the Helmholtz equation, see for example [10, 27]. An incoming wave that is scattered by an obstacle with boundary Γ results in a scattered field $u^{\mathrm{s}}(\mathbf{x})$ that can be represented by the so-called *single layer potential*,

$$u^{\mathrm{s}}(\mathbf{x}) = \int_\Gamma K(\mathbf{x},\mathbf{y})v(\mathbf{y})ds(\mathbf{y}). \tag{1}$$

Here, $K(\mathbf{x},\mathbf{y})$ is the Green's function of the Helmholtz equation with wavenumber k and $v(\mathbf{y})$ is the unknown *density function*, defined on Γ. Sound-soft and sound-hard obstacles give rise to Dirichlet or Neumann boundary conditions respectively, with zero pressure or zero normal velocity on Γ. Though other representations of the scattered field exist, in this paper we present our results for the following integral equation of the first kind with a Dirichlet boundary condition:

$$\int_\Gamma K(\mathbf{x},\mathbf{y})v(\mathbf{y})ds(\mathbf{y}) = -u^{\mathrm{inc}}(\mathbf{x}), \quad \forall \mathbf{x} \in \Gamma. \tag{2}$$

The function $u^{\mathrm{inc}}(\mathbf{x})$ in the right hand side represents an incoming wave, and the integral equation expresses that the total field $u^{\mathrm{tot}}(\mathbf{x}) = u^{\mathrm{s}}(\mathbf{x}) + u^{\mathrm{inc}}(\mathbf{x})$ vanishes on the boundary of the domain. Similar results can

*daan.huybrechs@cs.kuleuven.be
†peter.opsomer@cs.kuleuven.be

be obtained for other integral equations, as the approach does not depend on the particular equation – it depends on the asymptotic locality of the integral operator.

The discretization of $v(\mathbf{y})$ in (2) results in a boundary element method. It is a highly oscillatory function, thus requiring many degrees of freedom. In order to resolve all the oscillations of the problem, we follow a standard rule of thumb and choose a number of degrees of freedom N that is proportional to the wavenumber k in 2D, and proportional to k^2 in 3D. A collocation or Galerkin discretization of (2) results in a linear system

$$Ac = b, \tag{3}$$

where b represents the boundary condition. For both kinds of discretizations, the matrix A is dense, large and increasingly ill-conditioned. The relationship between the condition number and the wavenumber is complicated, and depends on properties of the obstacle and of the integral operators, see [7, §5] and [20]. It should be noted that integral equations of the second kind are more popular in applications because they are typically better conditioned for increasing N. However, the condition number also deteriorates with increasing wavenumber.

A fast matrix-vector product with A in the high-frequency regime is achieved by the high-frequency Fast Multipole Method [23, 16, 9, 28]. Alternatively, so-called hybrid numerical-asymptotic methods aim to significantly reduce the size of the linear system by incorporating information about the solution from asymptotic analysis (see the review [7] and references therein). In particular, phase-extraction methods use information about the phase g of the solution $v(\mathbf{y})$ in order to discretize only the remaining non-oscillatory part f in the following factorization:

$$v(\mathbf{y}) = f(\mathbf{y}, k)e^{ikg(\mathbf{y})}.$$

Phase extraction methods are simplest for convex obstacles, and require ray-tracing or similar techniques for more complicated domains or multiple scattering configurations [6, 13, 12, 1, 17, 8]. These methods typically lead to matrices that are small, sometimes with frequency-independent size, but that are still dense. The use of specialized quadrature methods for highly oscillatory integrals in [19] led to a matrix that is both small and sparse.

The goal of this paper is to explore the use of asymptotic properties of the integral operator, but without performing phase extraction. In doing so, we aim for greater generality and flexibility in the shape of the domain. The methodology of our approach is as follows. The linear system (3) represents the action of an oscillatory integral operator (discretized in A) on an oscillatory function (discretized in c). Hence, the product of a row of A with the column vector c discretizes a highly oscillatory integral. Without ray-tracing methods and phase estimation, the phase of the oscillations of this integral is unknown. Yet, each highly oscillatory integral of this kind is essentially local in nature, and one can localize oscillatory integrals explicitly using smooth cut-off functions. Conceptually, in our setting this corresponds to modifying the Green's function, or more generally the kernel of the integral equation at hand. That is, we replace $K(\mathbf{x}, \mathbf{y})$ by

$$\tilde{K}(\mathbf{x}, \mathbf{y}) = K(\mathbf{x}, \mathbf{y})w(\mathbf{x}, \mathbf{y}), \tag{4}$$

where $w(\mathbf{x}, \mathbf{y})$ is a smooth window function, or a sum of smooth window functions. This results in a modified discretization matrix $\tilde{A}$. The integral operator with kernel $\tilde{K}$ agrees asymptotically with the original operator as long as $w(\mathbf{x}, \mathbf{y})$ equals 1 in regions that contribute to the oscillatory integrals, and smoothly decays to zero outside these regions. Using basis functions with compact support in the discretization, the corresponding entries of $\tilde{A}$ are exactly equal to those of A. For regions where $w(\mathbf{x}, \mathbf{y})$ vanishes, the entries of $\tilde{A}$ are exactly zero. In the intermediate regions, the entries of $\tilde{A}$ are perturbations of those of A.

The idea and implementation of this approach is fairly straightforward, and can be based on an existing BEM implementation. We have performed our computations in Matlab for 2D problems, and using the software package BEMPP in 3D [24]. Our implementation is publically available on GitHub [22] and a copy of the code can always be obtained from the authors. The main challenge is estimating suitable locations for the window functions. In principle, this still requires asymptotic analysis of the scattering problem, and this is complicated for complicated geometries. However, the task of locating windows is significantly simpler than determining phases of the solution. Indeed, some contributions to the oscillatory integrals

intrinsically correspond to reflections of rays in the scattering configuration. A large part of the matrix A can be discarded simply with a visibility criterion: rays can not extend between two parts of an obstacle if they can not 'see' each other.

This results in some compression for any obstacle, or indeed any combination of obstacles in a multiple scattering configuration. But the compression rate can be much improved still. We numerically measure the contibuting regions of the integrals at a moderate value of k, and extrapolate the location of the windows to a higher value of k. Their location is refined with every increase of k, resulting in higher compression rates for high-frequency problems in an overall fairly efficient frequency sweeping solver.

Aside from sparsifying A, another important observation is that the condition number of $\tilde{A}$ seems much lower than that of A itself. The lower condition number has a positive effect on the number of iterations required in an iterative solver for (3). Furthermore, we show that the method is robust in several ways. It is robust with respect to the geometry of the obstacle: some amount of compression can still be achieved even for near-trapping domains, which are a worst case for ray-tracing methods. It is also robust with respect to the order of the BEM discretization. In spite of the fact that the asymptotic analysis of oscillatory integrals is mostly based on C^∞ integrands, we show that asymptotic compression can be achieved even when $v(\mathbf{y})$ is discretized using piecewise linear or piecewise constant functions. In this case the oscillatory integrals that we localize are merely continuous or even discontinuous.

On the other hand, unlike ray tracing methods our method is not frequency independent. Also, similar to ray tracing, many parts of our calculations depend on the direction of the incident wave. The 3D results in this paper are limited as well, due to having to compute large and dense matrices at high frequencies. However, the sparsifying modification of the Green's function is compatible with the fast multipole method, and a more efficient implementation in 3D is a possible future research project.

The structure of the paper is as follows. We review asymptotic properties of oscillatory integrals in § 2, and describe our method in more detail. The method is illustrated in § 3 with a basic 2D problem on a circle, of which we have full asymptotic knowledge. Here, we show that the number of nonzero entries in A can be reduced from $\mathcal{O}(k^2)$ to $\mathcal{O}(k^{3/2})$. We describe a proof-of-concept implementation in 3D, using a spherical obstacle, in § 4. Finally, in § 5 we describe several strategies for computing the location of the window functions for more general scattering configurations.

2 Asymptotic compression of BEM matrices

2.1 Oscillatory integrals

Oscillatory integrals of the form

$$\int_a^b f(x)e^{ikg(x)}\mathrm{d}x \tag{5}$$

are a classical topic in asymptotic analysis [5, 26]. The main result of relevance to us is that contributions to the integral originate in a small number of critical points. They include the endpoints of integration (a and b in the integral above), any singularities of the integrand and so-called stationary points. The latter are points p where the derivative of the phase function $g(x)$ vanishes, i.e. $g'(p) = 0$. Near a stationary point, the integrand is locally non-oscillatory. Elsewhere, oscillations cancel each other out. Asymptotically, the integral can be thought of as consisting of a sum of contributions, that can be isolated using smooth window functions.

Figure 1 shows the real part of $e^{ik(y-1/2)^2}$ with $k = 100$. This is a simple case of the general oscillatory integral above, with a stationary point at $p = 1/2$. The oscillations rapidly cancel out for high k, so that we can neglect all but a small region around the stationary point. We can evaluate this contribution by multiplying the integrand with a C^∞ window around $1/2$ and then integrating the nonzero part.

The asymptotic size of the contribution depends on the nature of the contributing point. The size of a stationary point contribution is typically $\mathcal{O}(k^{-1/2})$, whereas an endpoint contribution is smaller: $\mathcal{O}(k^{-1})$. Higher-order stationary points are points where higher order derivatives of g vanish as well. The more derivatives of g vanish, the less oscillatory the integrand and the larger the contribution. A stationary point

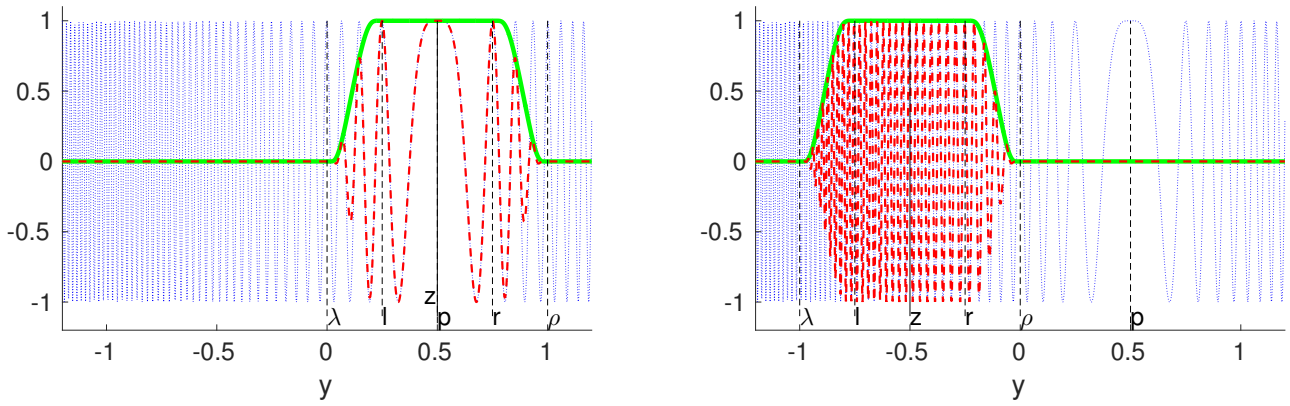

Figure 1: Illustration of the real part of the oscillatory integrand $e^{ik(y-1/2)^2}$ (dotted blue) with $k = 100$ and with a stationary point at $y = 1/2$. The stationary point contribution can be computed using a smooth window function (solid green) that covers it. The integral of the windowed function (dashed red) in the left panel asymptotically agrees with the integral of the oscillatory function. In contrast, the integral of the windowed function in the right panel is superalgebraically small in k.

p has order r if

$$g'(p) = g''(p) = \ldots = g^{(r)}(p) = 0$$

but $g^{(r+1)}(p) \neq 0$. The associated contribution to the integral has size $\mathcal{O}(k^{-1/(r+1)})$.

One typically uses C^∞ window functions in order to avoid introducing discontinuities in the derivatives of the integrand, as these would show up in the asymptotics. An extreme example of the latter is a block window on $[\lambda, \rho]$, which is discontinuous. This is equivalent to restricting an integral on $[a, b]$ to an integral on $[\lambda, \rho]$. Hence, one expects $\mathcal{O}(k^{-1})$ spurious contributions from the endpoints λ and ρ.

2.2 Asymptotic compression method

We consider a domain Γ that is parameterized by $\kappa : \mathcal{K} \to \Gamma$, such that the single layer potential becomes

$$\int_\Gamma K(\mathbf{x}, \mathbf{y}) v(\mathbf{y}) ds(\mathbf{y}) = \int_\mathcal{K} K(\mathbf{x}, \kappa(\tau)) \|\nabla \kappa(\tau)\| v(\tau) \mathrm{d}\tau.$$

In a slight abuse of notation, we identify $v(\mathbf{y})$ with $v(\tau)$. In the following, we shall also use a Green's function in the parameter domain as defined by

$$K_\kappa(t, \tau) = K(\kappa(t), \kappa(\tau)) \|\nabla \kappa(\tau)\|.$$

For the discretization we use a basis $\Phi_N := \{\varphi_j\}_{j=1}^N$, defined in the parameter domain $\mathcal{K}$, of compactly supported functions φ_j with support S_j. We intend to use piecewise polynomials. Hence,

$$v(\tau) \approx v_N(\tau) = \sum_{j=1}^N c_j \varphi_j(\tau). \tag{6}$$

This setting can easily be modified to one where Γ itself is approximated by elements, as is common in BEM.

With collocation at the points $x_i = \kappa(t_i)$, $i = 1, \ldots, N$, integral equation (2) leads to a discretization matrix A with entries

$$A_{i,j} = \int_{S_j} K_\kappa(t_i, \tau) \varphi_j(\tau) \mathrm{d}\tau.$$

We continue with the collocation discretization – Galerkin is entirely similar. Recall that a row of A times a column vector c represents an oscillatory integration and that these only have local contributions near

certain critical points. Assuming we know these, we make this explicit using a smooth bivariate windowing function w,

$$\tilde{K}_\kappa(t,\tau) = K_\kappa(t,\tau)w(t,\tau).$$

We introduce some more notation to specify w further. We divide the domain of w in three disjoint sets, $\mathcal{K}\times\mathcal{K} = \mathcal{K}_1 \cup \mathcal{K}_2 \cup \mathcal{K}_3$, such that

$$w(t,\tau) = \begin{cases} 1, & \text{if } (t,\tau) \in \mathcal{K}_1, \\ 0, & \text{if } (t,\tau) \in \mathcal{K}_3, \end{cases}$$

while $w(t,\tau)$ is C^∞ both in t and in τ.

Denote the compressed matrix corresponding to $\tilde{K}_\kappa$ by $\tilde{A}$, with entries

$$\tilde{A}_{i,j} = \int_{S_j} \tilde{K}_\kappa(t_i,\tau)\varphi_j(\tau)\mathrm{d}\tau = \int_{S_j} K_\kappa(t_i,\tau)w(t_i,\tau)\varphi_j(\tau)\mathrm{d}\tau.$$

It is clear that $\tilde{A}_{i,j} = A_{i,j}$ whenever $t_i \times S_j \in \mathcal{K}_1$, while $\tilde{A}_{i,j} = 0$ if $t_i \times S_j \in \mathcal{K}_3$. Recall that oscillatory integrals have only local contributions, so $\mathcal{K}_3$ will be large. This results in many zeros in $\tilde{A}$, hence *asymptotic compression*.

The matrix vector product $\tilde{b} = \tilde{A}c$ corresponds to the following oscillatory integral for $\tilde{b}_i$:

$$\tilde{b}_i = \sum_j \tilde{A}_{i,j}c_j = \int_{\mathcal{K}} K_\kappa(t_i,\tau)w(t_i,\tau)\sum_j c_j\varphi_j(\tau)\mathrm{d}\tau = \int_{\mathcal{K}} K_\kappa(t_i,\tau)w(t_i,\tau)v_N(\tau)\mathrm{d}\tau. \tag{7}$$

This integral asymptotically approximates the original one,

$$b_i = \sum_j A_{i,j}c_j = \int_{\mathcal{K}} K_\kappa(t_i,\tau)\sum_j c_j\varphi_j(\tau)\mathrm{d}\tau = \int_{\mathcal{K}} K_\kappa(t_i,\tau)v_N(\tau)\mathrm{d}\tau.$$

The values of these integrals do not agree in general. However, the assumption is that when v_N is an oscillatory function, and since the Green's function is oscillatory as well, for well chosen support sets κ_1 and κ_3 the two integrals for b_i and $\tilde{b}_i$ do agree asymptotically, i.e. up to some asymptotic error $\mathcal{O}(k^{-\alpha})$ where $\alpha > 0$.

We proceed by replacing A by $\tilde{A}$ in (3). This leads to a new linear system of equations,

$$\tilde{A}\tilde{c} = b,$$

with a sparse matrix $\tilde{A}$. For collocation, we simply have $b_i = -u^{\mathrm{inc}}(t_i)$. In this case, the weight function $w(t,\tau)$ need only be defined for the discrete points t_i.

2.3 Choice of the windows

The window function is a function of two variables, t and τ, but the integration is performed with respect to τ. Therefore, we consider the location of the window to be a function of t. In general, $w(t,\tau)$ is a sum of elementary window functions with locations depending on t:

$$w(t,\tau) = \sum_l \chi(\tau, \lambda_l(t), l_l(t), r_l(t), \rho_l(t)).$$

The specific choice of χ can be important from a numerical point of view, but we expect very similar results as long as all derivatives have a reasonable bound. The extreme case would be a block window ($\lambda = l$ and $r = \rho$), introducing the aforementioned spurious endpoint contributions. We choose χ as the elementary window also used in [6], and shown in Figure 1:

$$\chi(\tau,\lambda,l,r,\rho) = \begin{cases} 0, & \tau \le \lambda \\ \exp\left(\frac{2e^{\frac{\lambda-l}{\tau-\lambda}}}{\frac{\tau-\lambda}{l-\lambda}-1}\right), & \tau \in (\lambda, l) \\ 1, & \tau \in [l, r] \\ \exp\left(\frac{2e^{\frac{r-\rho}{\tau-r}}}{\frac{\tau-r}{\rho-r}-1}\right), & \tau \in (r, \rho) \\ 0, & \tau \ge \rho. \end{cases} \tag{8}$$

It is supported on $[\lambda, \rho]$ and it is equal to 1 on $[l, r]$. When two subsequent windows l and $l+1$ in w overlap or become too close, we join them into $\chi(\tau, \lambda_l, l_l, r_{l+1}, \rho_{l+1})$.

We have stated that our windows should include the critical points p of the oscillatory integral. We examine suitable locations further on in this paper. For the width of the window, it is customary to choose that depending on the order of the stationary point. As a rule of thumb, for a stationary point of order r the width of the window should scale like $\mathcal{O}(k^{-1/(r+1)})$. This implies in particular that the window can be smaller for larger frequency: the support is $\mathcal{O}(k^{-1})$ for an endpoint or an integrable singularity, $\mathcal{O}(k^{-1/2})$ for a simple stationary point, and $\mathcal{O}(k^{-1/3})$ for a stationary point of order two. In the setting of integral equations for scattering problems, the first case arises around the singularity of the Green's function and the second case around points of reflection of rays. The third cases arises around shadow boundaries: points where an incoming ray is tangential to the boundary are associated with second-order stationary points in asymptotic analysis [2]. These are also called points of grazing incidence.

2.4 Robustness for low-order discretizations

The asymptotic analysis of integrals of the form (5) usually assumes a smooth integrand. Typically, later terms in the asymptotic expansion depend on higher order derivatives of the integrand. Yet, in our setting we are faced with the discretized integral (7) that is not particularly smooth: the smoothness is limited at least by the smoothness of the basis functions φ_j. We can only expect low-order asymptotics because of the piecewise polynomial basis functions used in this article. In this sense, it is quite remarkable that the results further on show that asymptotic compression is also effective for piecewise linear or even piecewise constant basis functions, as smoothness of the integrand is important for asymptotic behaviour as $k \to \infty$.

This apparent robustness also allows for a significant simplification, that makes the implementation much cheaper. Rather than integrating the window function exactly, we will explore approximating the matrix element simply by multiplying with the window function:

$$\begin{aligned} \tilde{A}_{i,j} &= \int_{S_j} K_\kappa(t_i, \tau) w(t_i, \tau) \varphi_j(\tau) \mathrm{d}\tau \\ &\approx w(t_i, \tau_j) \int_{S_j} K_\kappa(t_i, \tau) \varphi_j(\tau) \mathrm{d}\tau \\ &= w(t_i, \tau_j) A_{i,j}. \end{aligned} \tag{9}$$

where τ_j is a point within the support of φ_j. This is a rather crude approximation of the integral, also depending on the choice for φ_j. However, it has the important advantage that the element of $\tilde{A}$ is a simple rescaling of the corresponding element of A. Thus, existing code for the computation of entries of A can maximally be reused.

Note that this approach is still decidedly different from simply compressing A by putting entries to zero. Even with our simplified approach, the elements of A are weighted, and thus decay to zero with some regularity.

3 Scattering by a circular obstacle

In this section we illustrate and explore the feasibility of asymptotic compression with a simple example, where we have full asymptotic knowledge of the behaviour of the solution. In particular, this allows us to decide a priori where the window functions should be supported.

3.1 Contributing points

Consider a 2D Helmholtz scattering problem from a disk with an incident plane wave coming from $x = -\infty$. With a disk of radius a, and its boundary parameterized by $\kappa(\tau) = a(\cos 2\pi\tau, \sin 2\pi\tau)$ for $\tau \in \mathcal{K} = [0, 1]$, the Green's function in the parameter domain is given by

$$K_\kappa(t, \tau) = \frac{i}{4} H_0^{(1)}(k\|\kappa(t) - \kappa(\tau)\|)\|\nabla\kappa(\tau)\| = \frac{i}{4} H_0^{(1)}(ka\sqrt{(\cos 2\pi t - \cos 2\pi\tau)^2 + (\sin 2\pi t - \sin 2\pi\tau)^2})2\pi a.$$

Here, k is the wavenumber of the Helmholtz equation and $H_0^{(1)}(z)$ is the Hankel function of the first kind and of order zero. This Green's function is oscillatory with its phase given by the Euclidean distance between $\kappa(t)$ and $\kappa(\tau)$. But this is not sufficient to determine the contributing points, since the density function is oscillatory too.

The asymptotic properties of scattering by a circular obstacle are well known [11, 19, 21]. There are three regions: the *illuminated region* is hit directly by the incoming wave, the *shadow region* is on the back side of the obstacle, and the *shadow boundary* is the transitional region in between. Note that these regions depend on the angle of the incoming wave – hence, so do the contributing points and so does our computational scheme. The regions and the corresponding contributing points are shown in Fig. 2.

Each collocation point has at least one critical point given by $\tau = t$, which corresponds to the singularity of the Green's function. For points in the illuminated region and in the shadow boundary this is the only one. It turns out that there is exactly one other critical point, a stationary point, when the collocation point lies in the shadow region. This point is not described in literature, but it arises as follows. One can assume the phase of $v(\tau)$ on the illuminated side is equal to the phase of the incident wave [19, Rem. 4.1]. The phase of $v(\tau)$ is thus equal to $r\cos(2\pi\tau)$ for $\mathbf{y} = \kappa(\tau)$ in the illuminated region, and the phase of $K_\kappa(t,\tau)$ is the Euclidean distance to the collocation point. Hence, there exists a slowly varying f such that

$$K_\kappa(t,\tau)v(\tau) = f(t,\tau,k)\exp[ikg(t,\tau)]$$

with

$$g = a\cos 2\pi\tau + a\sqrt{(\cos 2\pi t - \cos 2\pi\tau)^2 + (\sin 2\pi t - \sin 2\pi\tau)^2}$$

and therefore

$$\frac{\partial g}{\partial \tau} = -a\sin 2\pi\tau + a\frac{\sin 2\pi\tau\cos 2\pi t - \cos 2\pi\tau\sin 2\pi t}{\sqrt{(\cos 2\pi t - \cos 2\pi\tau)^2 + (\sin 2\pi t - \sin 2\pi\tau)^2}}.$$

The derivative of the phase is zero at $\tau = 1/2 - t$, hence $1/2 - t$ is a stationary point $\mathbf{p}$ of the integral (1). It lies in the illuminated region on the horizontal line through the collocation point, as shown in Figure 2.

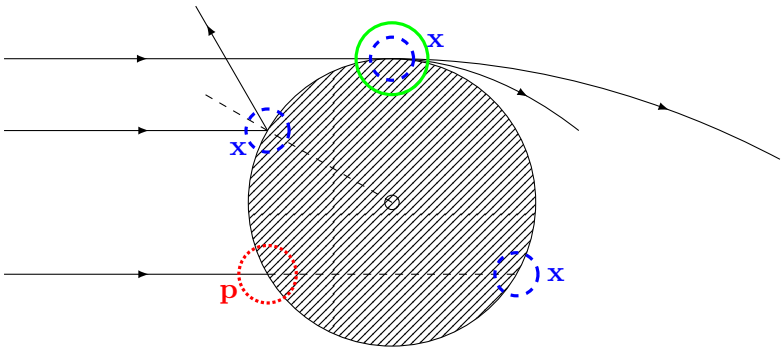

Figure 2: Illustration of the contributing points for three collocation points (blue dashed): a point in the illuminated region (top left), in the transitional shadow boundary region (top) and in the shadow (bottom right). The latter has a stationary point p in the illuminated region (red dotted). The width of the windows is $\mathcal{O}(k^{-1})$ for Green's singularities (blue), $\mathcal{O}(k^{-1/2})$ for a stationary point (red) and $\mathcal{O}(k^{-1/3})$ in the transition region (green).

Remark 1. *It holds more generally that for any collocation point in the shadow region, there is a stationary point in the illuminated region on the line connecting the collocation point with the source. As the density $v(\mathbf{y})$ is asymptotically very small in the shadow region, the integral in* (2) *needs a contribution from the illuminated region to satisfy the boundary condition. The ray does not physically go through the interior of the obstacle, but originates in that the Green's function only takes into account the distance between two points and not the location of that line.*

This is related to Fermat's principle, which states that rays travel along paths that minimize the total travel time, and is illustrated in Figure 3: the distance of a point source to a point $\mathbf{y}$ in the illuminated region

(which is the phase of the incident field there and also of the density $v(\mathbf{y})$) plus the distance of the latter to a point $\mathbf{x}$ in the shadow is minimal for that point lying on the line connecting the source to the shadow point. Our method for general geometries (see § 5.2 further on) confirms this and automatically recovers the stationary point.

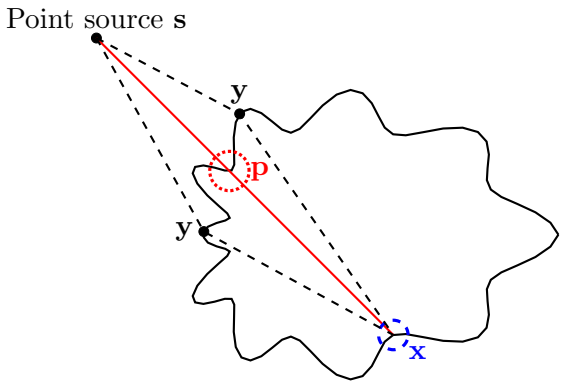

Figure 3: A collocation point in the shadow region ($\mathbf{x}$ in the figure) always has a stationary point $\mathbf{p}$ on the boundary in the illuminated region, that lies on the line connecting $\mathbf{x}$ to the source $\mathbf{s}$. By Fermat's principle this point minimizes the sum $\|\mathbf{s}-\mathbf{y}\|+\|\mathbf{y}-\mathbf{x}\|$ for $\mathbf{y}$ on the boundary.

3.2 Fixed windows without discretization

As a first experiment, we introduce window functions in the exact integral (1), i.e. without any discretization. This experiment confirms the validity of introducing window functions to localize the integral, and allows us to experiment with a suitable width of the window. We do need the exact solution $v(\mathbf{y})$ for this experiment, so we restrict ourselves to the aforementioned case of a circle where an exact solution is known.

The exact scattered field is given in [18] in terms of an expansion in Bessel functions and outgoing Hankel functions. At a point $\mathbf{x} = r(\cos 2\pi\sigma, \sin 2\pi\sigma)$ in the exterior field (i.e., $r > a$), we have

$$u^{\mathrm{s}}(\mathbf{x}) = kJ_0(ka)\frac{H_0^{(1)}(kr)}{H_0^{(1)}(ka)} + 2\sum_{n=1}^{\infty} i^n J_n(ka)\frac{H_n^{(1)}(kr)}{H_n^{(1)}(ka)}\cos(2n\pi\sigma). \tag{10}$$

From this we derive the density function of our integral equation formulation as the normal derivative along the boundary [10],

$$v(\tau) = kJ_0(ka)\frac{H_0^{(1)\prime}(ka)}{H_0^{(1)}(ka)} - ik\cos(2\pi\tau)\exp(ika\cos[2\pi\tau]) + 2k\sum_{n=1}^{\infty} i^n J_n(ka)\frac{H_n^{(1)\prime}(ka)}{H_n^{(1)}(ka)}\cos(2n\pi\tau). \tag{11}$$

In our experiments, we terminate this sum when $n > 1.7k + 50$ or when two consecutive terms are too small. We choose a few representative collocation points $\mathbf{x}_i = \kappa(t_i)$ on the boundary of the domain and evaluate the integrals

$$\int_0^1 w(p_i,\tau)K_\kappa(t_i,\tau)v(\tau)d\tau. \tag{12}$$

Here, p_i is a contributing point. In this experiment we chose $p_i = t_i$ for $\mathbf{x}_i$ in the illuminated region, while $p_i = 1/2 - t_i$ is the stationary point for $\mathbf{x}_i$ in the shadow region. We have chosen a window parameterized by $T > 0$, such that the window has total support $2T$ and it is equal to 1 on an interval of length T around the point p_i, i.e.:

$$w(t_i,\tau) = \chi(\tau, p_i - T, p_i - T/2, p_i + T/2, p_i + T).$$

The results are shown in Figures 4 and 5 for a circle with radius $a = 1/2$. The error decreases for larger window widths T, until ultimately T is large enough such that the window covers the entire boundary. In

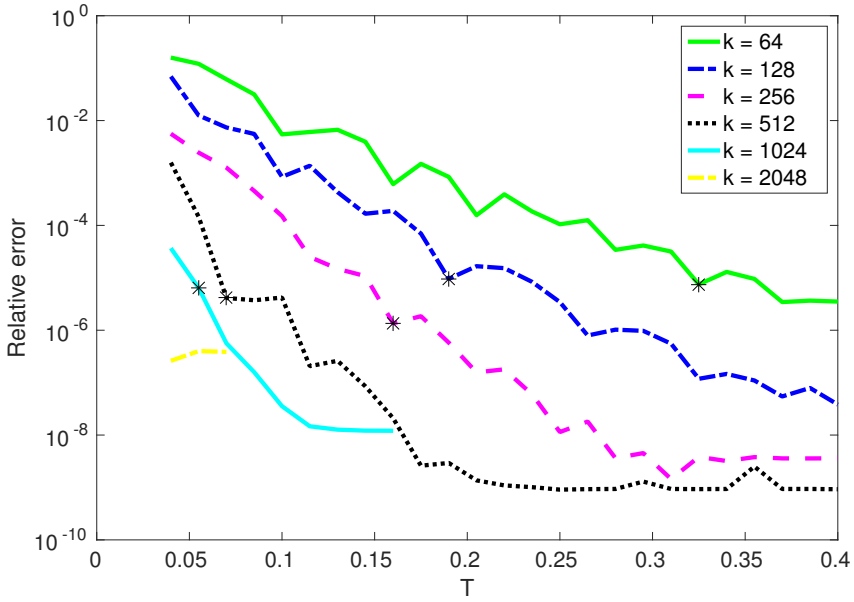

Figure 4: Relative error of the integral (12) with respect to the known field (10) as a function of the window width T for some wavenumbers k and $\mathbf{x}$ in the illuminated region.

that case, there is no more compression and the integral reduces to the classical case. Interestingly, the error also decreases rapidly with increasing wavenumber k and fixed T. This confirms that the windowed and non-windowed integrals asymptotically agree.

The data indicated by a black asterisk indicates the lowest T for which the error is smaller than 10^{-5} at each of the tested wavenumbers. This gives rise to the least-squares approximations shown in Figure 6, where we evaluate how the window width should scale with k in order to maintain an error below this threshold. As expected, the smallest rate of decrease is seen for points in the transitional region. The rate is in close agreement with the $\mathcal{O}(k^{-1/3})$ behaviour of the windows size that was suggested in § 3.4 for a stationary point of order 2. The other rates match as well, roughly: the results are slightly above $\mathcal{O}(k^{-1/2})$ for a point in the shadow (p_i is a stationary point of order 1 in the illuminated region), and below $\mathcal{O}(k^{-1})$ for the singularity of the Green's function in the illuminated region (like an endpoint). As the evaluation of the scattered field is also an oscillatory integral, we could introduce windows scaling with k into that integral as well.

3.3 Fixed wavenumber-independent windows in a BEM discretization

Next, we illustrate what happens when we introduce these windows in a classical BEM discretization. Here we compress the dense collocation matrix A into a sparse matrix $\tilde{A}$, but such that it still represents the integral operator (1) in an asymptotic sense.

We multiply the kernel with window functions with a fixed width $T = r - l = (\rho - \lambda)/2$ when centered around the Green singularities, and a larger width $3T$ around the stationary points. We take into account the periodicity of the integrand as well as continuity of the windows: when windows partially overlap they are combined into one.

Figure 7 shows the structure of $\tilde{A}$. Similar patterns were seen in [15, 19], based on phase extraction which we do not employ here. The singularity of the Green's function is present along the diagonal of the matrix. The upper right and lower left corners are also included due to the periodicity. The wider bands in the anti-diagonal direction correspond to the stationary point in the illuminated region, for a collocation point in the shadow (recall that we have used a wider window for these contributions, hence the wider band). Some sparsity is observed: $\tilde{A}$ has only 36.0% nonzeros for a wavenumber as small as $k = 256$, using $N = 6k$ and $T = 0.08$. This also gives a 0.776% relative error on the solution vector c. We also evaluated how well the scattered field matches the boundary conditions in 100 points spread along the boundary. This error

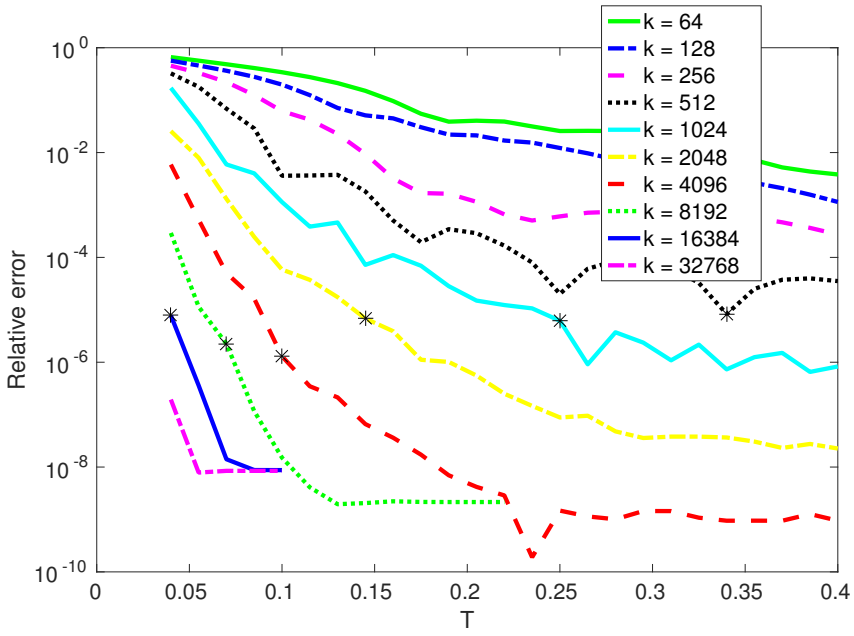

Figure 5: Relative error of the integral (12) with respect to the known field (10) as a function of the window width T for some wavenumbers k and $\mathbf{x}$ in the shadow region.

increases very slightly from 1.79% to 2.01% on average. This experiment confirms that, at least for this simple example, one can introduce sparsity in the BEM matrix at virtually no cost in accuracy.

We repeated the experiment with a much simpler compression scheme. We simply discard all elements of A when they were zero in $\tilde{A}$ above, but without changing the other entries of A. This corresponds closely to using a block window function, rather than the smooth function (8). Recall from §2.1 that this would introduce spurious $\mathcal{O}(k^{-1})$ endpoint contributions for a general oscillatory integral. Yet, we observe only 11.4% error on c and 6.22% error on the averaged boundary conditions. This error is larger than before, but still not excessively large. The reason, at least in this case, is that the contributions of the Green's singularity and stationary point dominate. The spurious contributions caused by the discontinuous compression scheme are more than an order of magnitude smaller.

Using the smooth windows again, we vary the wavenumber k and the window size T in Figure 8. Increasing T lowers the error as in § 3.2, but also reduces sparsity. We have used cubic splines φ_j in this experiment. Results are similar when using linear basis functions, but a saturation error of about 10^{-2} is

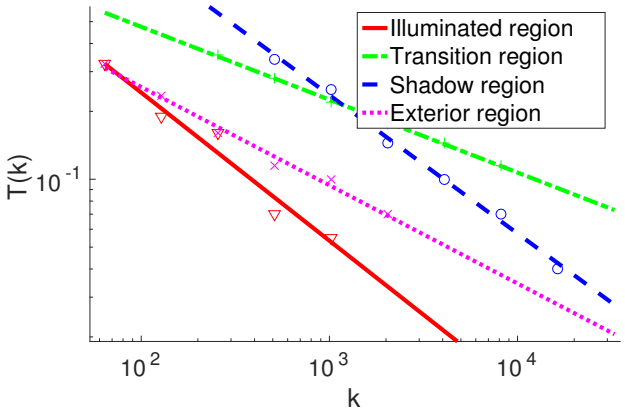

Figure 6: Estimated required window sizes as a function of frequency to achieve a relative error $< 10^{-5}$ for an illuminated point, a transition point, a shadow point and an external point.

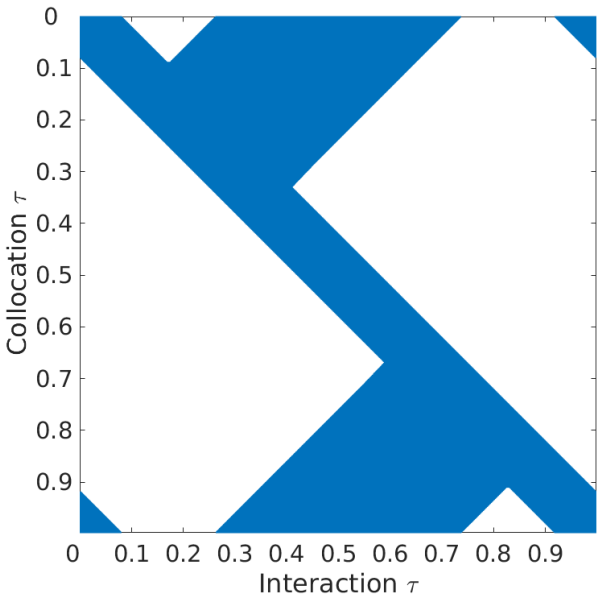

Figure 7: Sparsity structure of $\tilde{A}$ for the circle, $k = 256$ and $T = 0.08$.

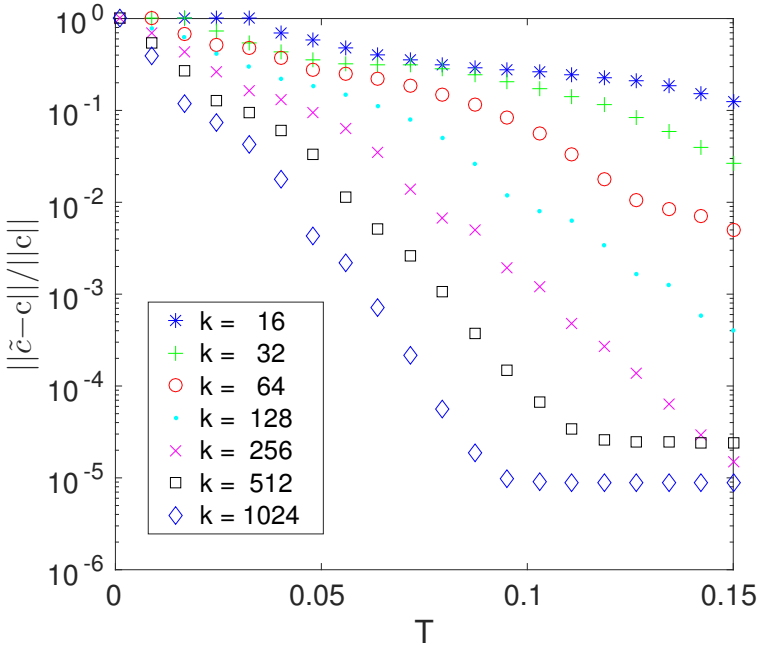

Figure 8: Relative error on the solution vector c for varying T and k for cubic basis functions.

observed at moderate T. This corresponds to the discretization error of the BEM discretization, and one can not expect to improve on that.

3.4 Complexity reduction: varying the window width with k

Until now we have used a window function of fixed size, independent of k. As a result, the percentage of non-zero elements in $\tilde{A}$ remains fixed as k increases. However, the theory of oscillatory integrals predicts one can decrease the window size with k, resulting in higher compression ratios at higher frequencies. In turn this results in a matrix-vector product with a lower computational complexity for large k. As a final experiment for the case of a circular scatterer, we use our knowledge of the contributing regions to shrink the windows with increasing k.

We use windows with width $\mathcal{O}(k^e)$ as indicated in Figure 2, with $e = -1, -1/2$ or $-1/3$ depending on the nature of the contributing point. Each collocation point corresponds to a row of the discretization matrix. There is always a Green singularity, for which we use an $\mathcal{O}(k^{-1})$ window in the physical domain. The width of the window decreases, but the number of points increases with $N = \mathcal{O}(k)$, and as a result each such window covers $\mathcal{O}(Nk^{-1}) = \mathcal{O}(k^{1-1}) = \mathcal{O}(k^0)$ points. This leads to $\mathcal{O}(k^0)$ nonzero entries in each row, and $\mathcal{O}(Nk^0) = \mathcal{O}(k)$ nonzero elements in the matrix in total. Furthermore, $N/2$ collocation points in the shadow region require an additional $\mathcal{O}(k^{-1/2})$ window around their stationary points. By the same reasoning, this leads to $\mathcal{O}(NNk^{-1/2})$ nonzero entries in the matrix. Finally, for points in the transition region we use larger $\mathcal{O}(k^{-1/3})$ windows, but we can assume that there are only $\mathcal{O}(N^{2/3})$ points in this region because the transition region itself shrinks like $\mathcal{O}(k^{-1/3})$ [19]. The total number of nonzeros is $\mathcal{O}(NNk^{-1}) + \mathcal{O}(NNk^{-1/2}) + \mathcal{O}(N^{2/3}Nk^{-1/3}) = \mathcal{O}(k^{3/2})$.

Indeed, the percentage of nonzeros in the computed $\tilde{A}$ decreases by a factor that approaches $1.46 \approx \sqrt{2}$ each time k is doubled and reaches 11.8% at the highest wavenumber $k = 2^{12}$. Of course, this complexity is by design since we have chosen the scaling of the size of the window functions as above. More importantly, Table 1 shows that the error remains approximately constant with increasing k in this approach. In this experiment, using cubic basis functions $\varphi_j(\mathbf{y})$ leads to the same qualitative results as using linear ones.

The error can be reduced by increasing the constants in front of k^e, i.e. by choosing larger windows. In practice, it can also be advantageous to use non-symmetric window functions. We illustrate a few integrands

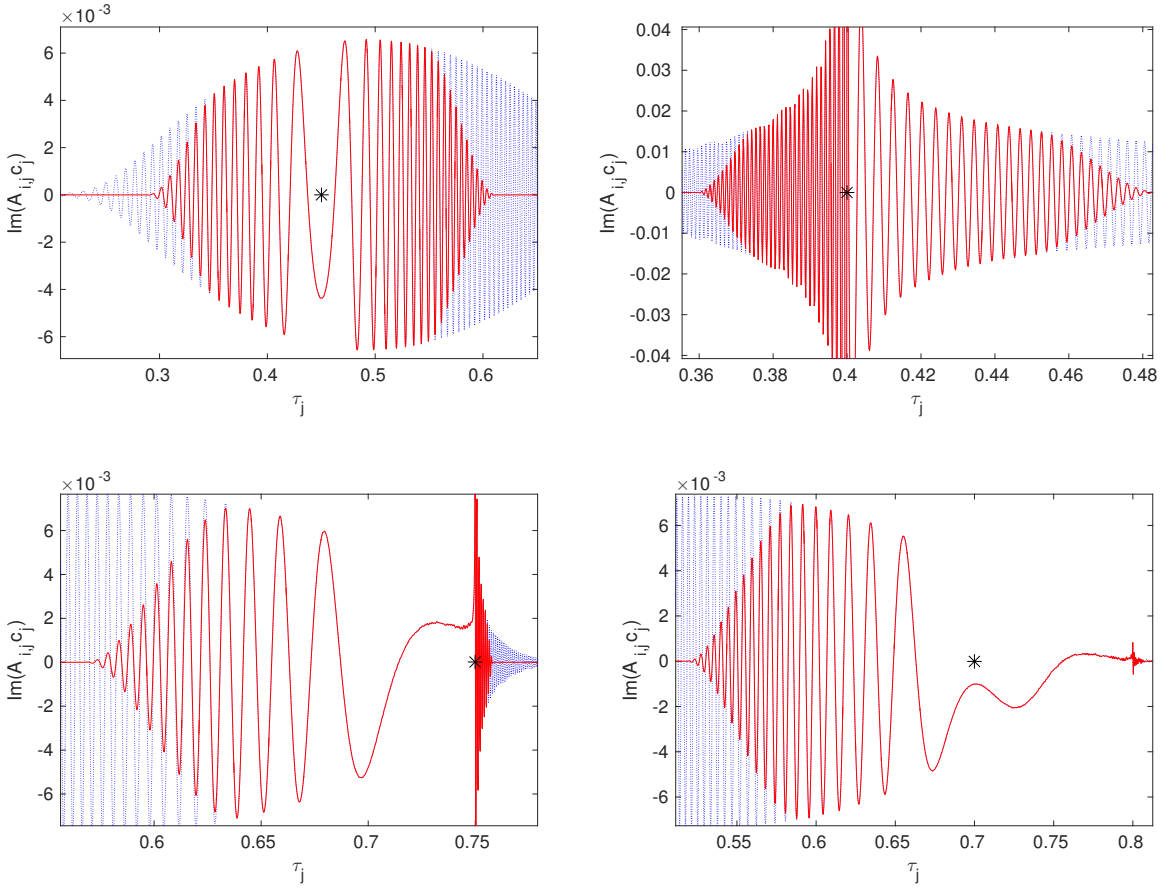

Figure 9: Discretized integrand (blue dotted) and windowed version (red line) for cubic basis functions $\varphi_j(\mathbf{y})$ at $k = 1024$ for four contributing points (black asterisks): a stationary point in the illuminated region (top left), a Green's singularity in the illuminated region (top right), the lower transitional point (bottom left) and a stationary point in the lower transitional region (bottom right).

of the windowed and non-windowed integrals in Figure 9. For example, the bottom left shows that the integrand is locally very nonoscillatory only to the left of the transition point $\tau_i = 3/4$. This allows using a $\mathcal{O}(k^{-1})$ window to the right, as was done for the results shown in this section.

Finally, we evaluate the condition numbers of the matrices A and $\tilde{A}$. Figure 10 (left panel) shows that the condition number improves significantly after compression. This allows for a faster solution using an iterative solver. We have used the non-restarted `gmres` solver of Matlab with tolerance 10^{-5} to solve the linear systems $Ac = b$ and $\tilde{A}c = b$, using linear and cubic basis functions. The number of iterations to convergence are shown in the right panel of Figure 10. Asymptotic compression has a clearly beneficial effect on the total number of iterations, and this effect is more pronounced for the linear basis functions.

4 Scattering by the unit ball

The principles underlying the asymptotic compression scheme are valid in higher dimensions as well. In this section, we perform a limited experiment to illustrate the validity of the asymptotic compression scheme in 3D. A more involved exploration of 3D problems is a topic of further research.

4.1 Galerkin discretization of a spherical obstacle

We illustrate the performance of our compression method in 3D by applying it to scattering off a unit ball using the openly available software package BEMPP [24].

k		16	32	64	128	256	512	1024	2048	4096
L	$\frac{\|\tilde{c}-c\|_2}{\|c\|_2}$	0	1.41e-3	9.62e-4	9.49e-4	3.91e-3	7.48e-3	2.74e-3	4.65e-3	6.48e-3
C	$\frac{\|\tilde{c}-c\|_2}{\|c\|_2}$	0	8.09e-4	1.06e-3	6.91e-4	6.57e-4	4.95e-4	3.16e-4	2.39e-4	3.81e-4
L	$\frac{\|Ac-b\|_2}{\|b\|_2}$	6.41e-16	4.98e-4	4.48e-4	4.80e-4	1.88e-3	3.49e-3	2.11e-3	3.43e-3	4.09e-3
C	$\frac{\|Ac-b\|_2}{\|b\|_2}$	6.60e-16	2.38e-4	2.95e-4	3.21e-4	3.13e-4	2.52e-4	1.86e-4	1.75e-4	2.71e-4

Table 1: Relative error on the solution vector and compression errors when applying complexity reduction on the circle for linear (L) and cubic (C) basis functions $\varphi_j(\mathbf{y})$.

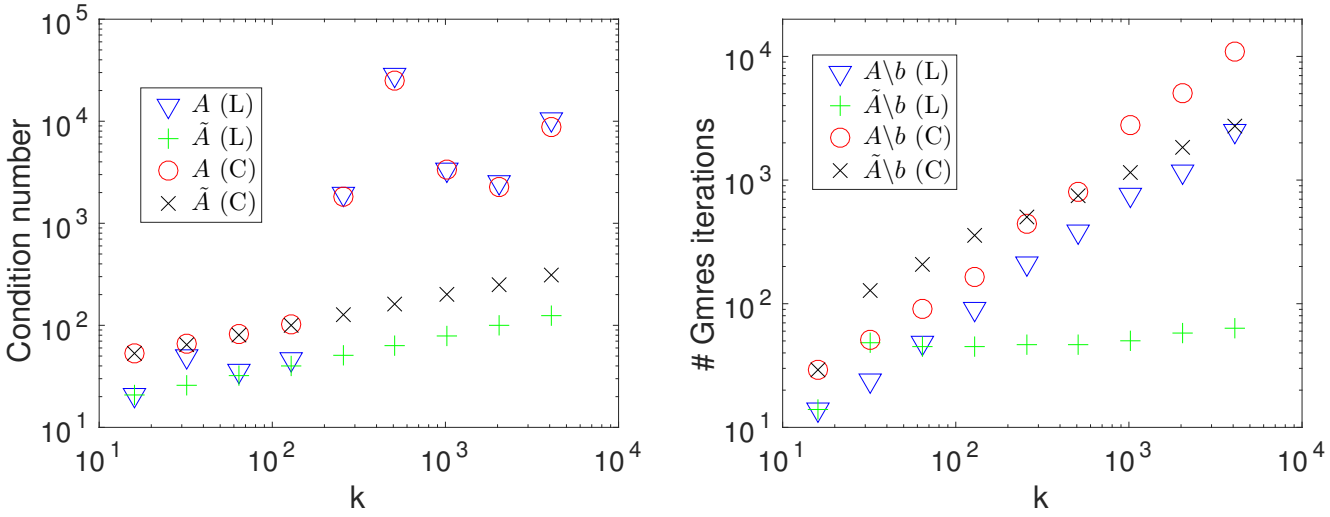

Figure 10: Condition numbers and number of GMRES iterations as a function of the wave number when applying complexity reduction on the circle for linear (L) and cubic (C) basis functions $\varphi_j(\mathbf{y})$.

Motivated by the reasonable results when using piecewise linear basis functions in 2D, in spite of the typical smoothness of integrands that is assumed in asymptotic analysis, we stretch the limits and choose piecewise constant basis functions in 3D. We have used a mesh of the unit sphere with 3219 piecewise constant triangular elements for $k = 8$ and approximately four times more elements for $k = 16$. We respect the scaling $N = \mathcal{O}(k^2)$ for the total number of degrees of freedom for larger wavenumbers.

The BEMPP software is based on Galerkin discretization, and hence we adapt our scheme to use Galerkin rather than collocation. This change only affects the choice of the window function: in a collocation scheme we only have to choose a suitable window for each collocation point t_i, whereas in a Galerkin scheme, t is a continuous variable in the window $w(t, \tau)$. In order to avoid this additional complexity, and since we are dealing with a non-smooth integrand anyway, we can simplify the computation of matrix entries considerably using the technique suggested in §2.4 and in particular equation (9). That is, rather than recomputing the matrix entries using windowed integrands, we simply use the matrix elements as computed by BEMPP and weigh them according to the window function:

$$\begin{aligned}\tilde{A}_{i,j} &= \int_{S_i}\int_{S_j} K_\kappa(t,\tau)w(t,\tau)\phi_j(\tau)\phi_i(t)\|\kappa(t)\|\,\mathrm{d}\tau\,\mathrm{d}t \\ &\approx w(t_i,\tau_j)\int_{S_i}\int_{S_j} K_\kappa(t,\tau)\phi_j(\tau)\phi_i(t)\|\kappa(t)\|\,\mathrm{d}\tau\,\mathrm{d}t \\ &= w(t_i,\tau_j)A_{i,j}. \end{aligned} \tag{13}$$

Here, we choose the points t_i and τ_j to be the centers of S_i and S_j, the supports of the basis functions φ_i and φ_j. This crude approximation is very practical, yet experiments indicate it is nearly as accurate for the

overal solution error as when computing the windowed integrals (see §4.3 below). The overal error is usually dominated by the discretization error, not by the asymptotic compression error.

4.2 Compression and convergence for small wavenumbers

We consider a plane wave incidence in the x-direction, analogously to § 3.1 for scattering by a disk. The asymptotic behaviour of the solution is rather similar. There are no stationary points of the integrand when $\kappa(t)$ lies in the illuminated region. There is a single stationary point in the illuminated region when t is in the shadow, and the stationary point has the same y and z coordinate as $\kappa(t)$.

For simplicity and because of lack of a natural ordering, we have defined a window function in space, rather than in the parameter domain as before. The window depends on a parameter T that determines its size, and is shaped like a ball around the point $\mathbf{x} - \mathbf{y}$:

$$w(\mathbf{x}, \mathbf{y}) = \chi\left(\sqrt{(x_x - x_y)^2 + (y_x - y_y)^2 + (z_x - z_y)^2}, 0, 0, 0.8T, T\right).$$

For the purposes of our experiment, a more convenient choice is

$$w(\mathbf{x}, \mathbf{y}) = \chi\left(\sqrt{(y_x - y_y)^2 + (z_x - z_y)^2}, 0, 0, 0.8T, T\right).$$

since that window represents a circular tube in the x-direction through the obstacle that automatically includes the stationary point in the illuminated region when t is in the shadow (since the y and z coordinates of t and its stationary point agree).

Figure 11 shows that the condition number improves markedly when T is small. Figure 12 shows that the relative error behaves similar to the 2D case in Figure 8: the error decreases with increasing support size T, and the error is smaller for larger k (at least for small T). We verified that the average error on 100 boundary conditions (the integral operator applied to the computed density minus the Dirichlet boundary condition, evaluated at a point on the obstacle) also decreases to 4% as T increases, because the windows grow to cover the entire domain. That same error is observed in the case without compression.

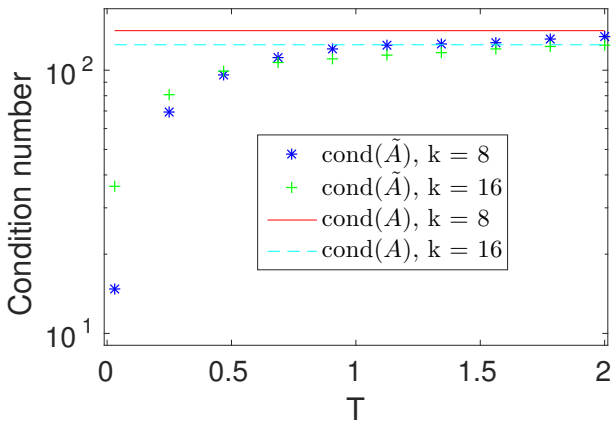

Figure 11: Condition number of the 3D example.

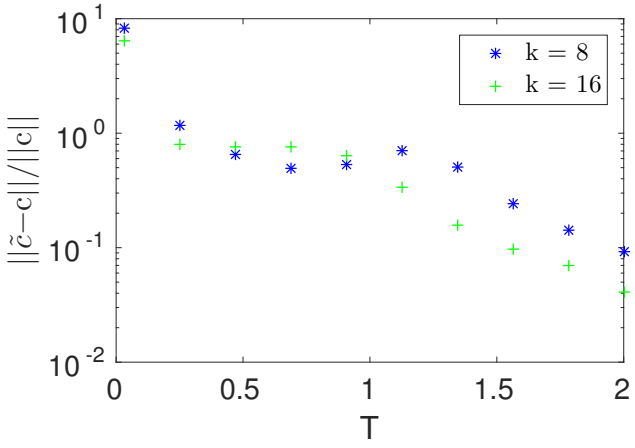

Figure 12: Relative error on the solution vector c in the 3D example.

Yet, for small T the errors are rather large and this is due to the fact that the wavenumbers are too small to observe asymptotic error decay. Using larger meshes at higher wavenumbers gives rise to memory issues in our direct implementation, when initialising A or $\tilde{A}$ as a full $N \times N = \mathcal{O}(k^4)$ matrix. For the latter, it should be possible to use another representation such as a $\mathcal{H}^2$ matrix. Thus, memory usage would reduce significantly and the hierarchical structure allows checking more efficiently whether $\mathbf{y}$ is in the support of $w(\mathbf{x}, \mathbf{y})$. This approach is very interesting, but beyond the scope of the current article. Instead, we will illustrate asymptotic accuracy of the scheme for larger wavenumbers using the fact that we know the exact solution.

4.3 Compression accuracy at larger wavenumbers

In order to avoid having to compute an expensive reference solution of the scattering problem at larger wavenumbers, we restrict ourselves to a limited experiment using the known exact solution. First, we compute a reference solution by projecting the analytical solution onto the discretization space of piecewise constant functions. Next, we compute a full row of the discretization matrix and a compressed one, and assess the corresponding error in the matrix-vector product.

We approximate the solution vector c by $\bar{c}$ without constructing A, by projecting the normal derivative of the known solution onto the grid. In the case of a unit sphere, Dirichlet boundary conditions and an incident plane wave in the x-direction, one can use spherical harmonics (see [18, pg. 292-294] for the Neumann case) to solve the Helmholtz problem:

$$v(\mathbf{y}) = -ikx_y e^{ikx_y} + \sum_{n=0}^{\infty}(2n+1)ki^n \frac{j_n(k)h_n^{(1)\prime}(k)}{h_n^{(1)}(k)} P_n(x_y).$$

Here, we use the spherical Bessel function, the spherical outgoing Hankel function and the Legendre function ($P_n(1) = 1$), where x_y denotes the x-coordinate of $\mathbf{y}$. Using piecewise constant basis functions $\varphi_i(y)$, and truncating the infinite sum after numerical convergence, we obtain the expression

$$\bar{c}_l = \left[\int_l \varphi_l(y) \left(\left\{ \sum_{n=0}^{1.4k+40} (2n+1)ki^n \frac{j_n(k)h_n^{(1)\prime}(k)}{h_n^{(1)}(k)} P_n(x_y) \right\} - ikx_y e^{ikx_y} \right) dy \right] \left(\int_l \varphi_l(y) dy \right)^{-1}, \tag{14}$$

where the integration is over a triangular element l. We refine the mesh in each spatial dimension as the wavenumber increases using Gmsh [14].

The accuracy of our reference solution is illustrated in Table 2. We apply the integral operator to the density function and evaluate at a point on the boundary. This value is compared to the boundary condition at 40 points placed along the sphere. The error is roughly constant for increasing wavenumber, and it matches the discretization error of the integral operator.

k	8	16	32	64	128	256
Error on BC	0.0383	0.0356	0.0341	0.0338	0.0317	0.0276

Table 2: Average relative error the boundary conditions on 40 points on the sphere when using (14).

We have computed a number of rows of the dense matrix A, as well as of the compressed matrix $\tilde{A}$ using (13). The exact matrix-vector product with the solution vector c would be $Ac = b$, and our projection approximation above yields $A\bar{c} = \bar{b}$. Using the compressed matrix $\tilde{A}$ we have the approximation

$$\tilde{A}\bar{c} = \tilde{b}.$$

We can compute the exact right hand side b_i, since it is determined by the boundary condition.

In Figure 13 we show the relative error of the compressed matrix-vector product element $\tilde{b}_i$ compared to the exact one b_i,

$$\left| \frac{b_i - \tilde{b}_i}{b_i} \right|.$$

For reference, the figure also includes the relative error of $\bar{b}_i$ versus b_i ('Full row'). These values correspond to the results in Table 2 and they are indicative of the discretization error.

In this approach, we can cheaply consider larger wavenumbers. We have used a row corresponding to φ_i in the illuminated region in the left panel of Figure 13, and in the shadow region in the right panel. In the latter case, the major contribution to the integral comes from a stationary point in the illuminated region. The results show that the error decreases with increasing k in both cases. We have illustrated different values of T, the width of the window function. The error is intially larger for smaller T, but still converges to the level of the discretization error for increasing k. The convergence is slower for the case of the shadow region,

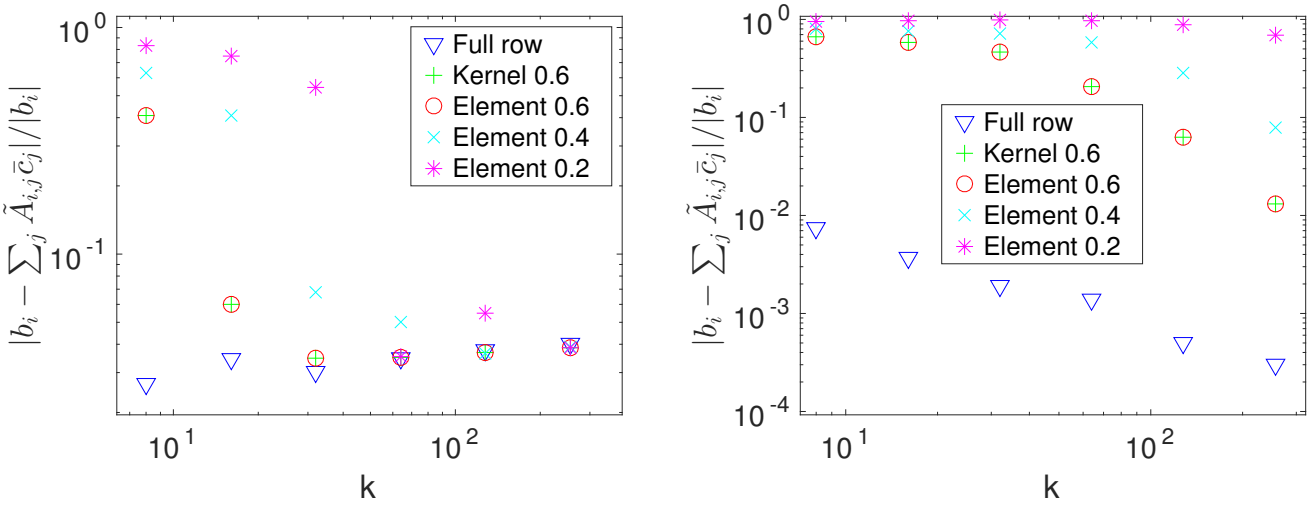

Figure 13: Relative error, as a function of the wavenumber, of the matrix vector product $Ac = b$ for a row i corresponding to φ_i supported in the illuminated region (left panel) and in the shadow region (right panel). 'Full row' means we do not use a windowed integral, 'Kernel 0.6' means we integrate the windowed kernel function with $T = 0.6$, and 'Element 0.2' means we use approximation (13) with $T = 0.2$.

but recall from the 2D experiment that a stationary point requires a larger window and we are comparing the same support in these results.

Finally, the figure also includes the results when integrating the windowed integrand, rather than using the approximation (13). It shows that no accuracy is lost when using the much cheaper approximation (14), as the results are very close to each other. In fact, the errors for $T = 0.6$ agree up to at least seven digits, which is the case for $k = 8$.

5 More general geometries in 2D

Asymptotic compression is more interesting in the absence of a priori asymptotic information, since otherwise true asymptotic methods could be used. In this section, we explore three ways to estimate suitable locations of the window functions. The first approach is based on geometrical considerations. In the second and third approach, we use a solution at a smaller frequency to automatically select windows for higher frequency problems.

Throughout this section, we use piecewise linear basis functions and we perform experiments in 2D using the obstacles shown and named in Figure 14. These include highly non-convex and multiple scattering configurations. We will illustrate different aspects of our methods with these different scattering configurations.

5.1 Visibility criterion

Asymptotically, a wave field can be seen as a collection of rays along straight paths (in a homogeneous medium) [3]. Points of reflections of these rays physically correspond to stationary points in the integral equation formulation. For scatterers with a moderately complicated geometry, it becomes unwieldy to trace all reflecting rays through the scene. However, in the integral equation formulation, the oscillatory integral in equation (2) corresponding to a point $\mathbf{x} \in \Gamma$ on the boundary always asymptotically corresponds to a sum of contributions from a limited number of points.

If a point B on the boundary is not directly visible from a point A on the illuminated part of the boundary, then B can not be a stationary point of the oscillatory integral at A. Indeed, there can be no direct ray from B to A (or vice-versa). There can only be indirect connections via intermediate reflection points elsewhere on the boundary, or via creeping rays along the surface of the obstacle. This means that

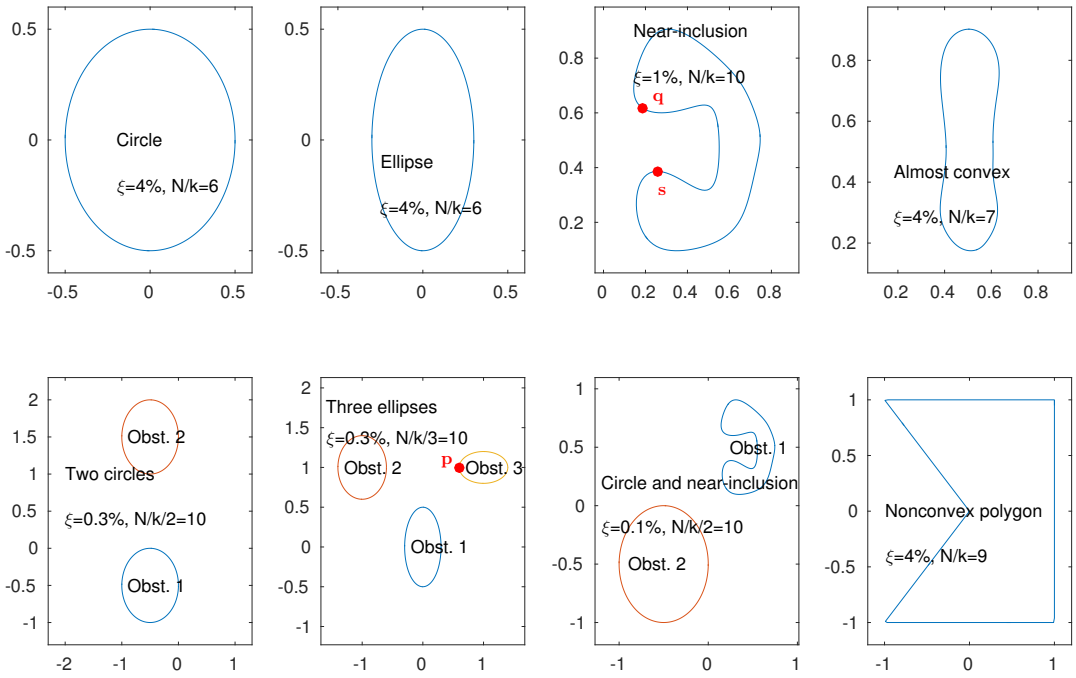

Figure 14: Obstacles with their respective names, threshold percentages ξ and relative number of points used in this section, with some indicated points.

for any given point A on the illuminated part of the boundary, we can asymptotically discard the density in all non-visible parts of the boundary from that point A. This reasoning does not immediately hold for points on the shadow side of the boundary, for which the situation is more complicated.

In a collocation solver, we have to decide for each collocation point t_i where to place the window function $w(t_i, \tau)$. For objects with self-reflections, one could trace a ray from the source through the scattering scene to the collocation point, much like ray tracing in computer graphics. Each point of reflection is expected to be a stationary point for the next point of reflection, or ultimately for the collocation point. Hence, each of these points needs a window around it, and any two subsequent points have to be able to 'see' each other for a reflection to be possible. In the next experiments, we do not consider any ray tracing, but simply exploit the latter visibility condition. Computing which points can see one another gives the regions where critical points can lie. The visibility problem is also common in computer graphics, and the computation can be sped up using Kd-trees or Bounding Volume Hierarchies [25].

Results are shown for a near-inclusion domain in Figure 15. The collocation point given by the parameter value $\tau = 1/2$ in the figure can only have stationary points in the thick blue region, appended by a small blue-dashed region where the window function can smoothly decay to zero. The remainder of the boundary gives no contributions to this point.

The full sparsity pattern of the compressed matrix is illustrated in Figure 16, where we have used the visibility criterion for all collocation points in the illuminated region. The near-inclusion of the domain corresponds to a dense square in the middle of the matrix. This square resolves all the scattering going on inside the cavity, but it is (asymptotically) independent from the scattering going on outside. Collocation points with τ approximately in $[0.2, 0.3]$ or $[0.7, 0.8]$, where the obstacle is locally convex, can only 'see' themselves. This leads to a small band around the diagonal in the discretization. In total, the visibility condition leads to 60.1% nonzero elements in $\tilde{A}$ at a wavenumber as small as $k = 2^8$. The relative error of $\tilde{c} = \tilde{A}^{-1}b$ with respect to the exact solution vector $c = A^{-1}b$ is 13.3%, for a plane wave incidence from the left. The condition number improves approximately half an order of magnitude, from $7.65e2$ to $1.53e2$.

This approach could be made automatic and more robust, and whether two points can 'see' each other is

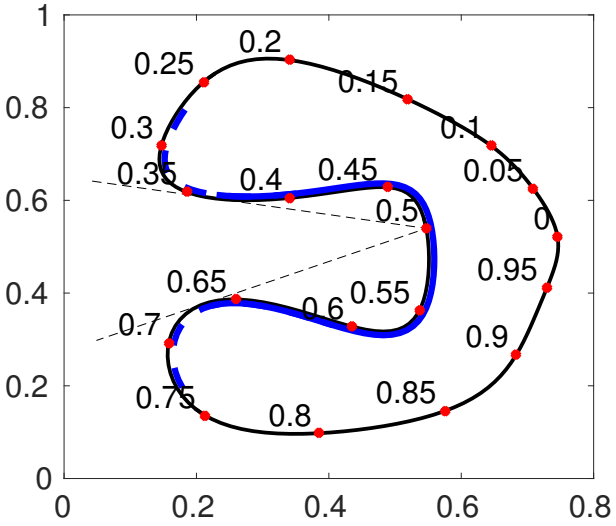

Figure 15: Obstacle, parametrisation and region which is visible from $\tau = 1/2$.

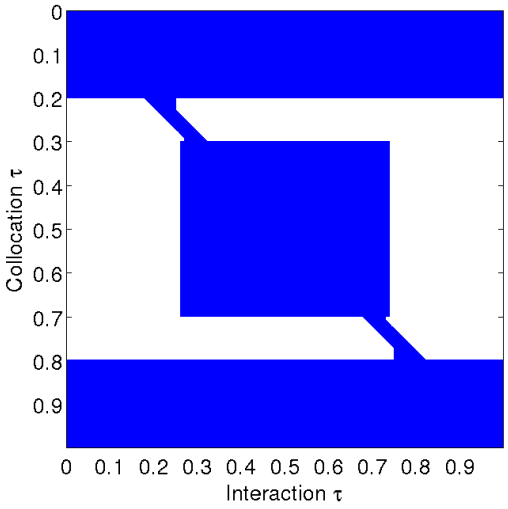

Figure 16: Structure of the compressed matrix using the visibility criterion and Figure 15.

independent of the incident wave. However, one can only gain a percentage of nonzeros that is independent of k and which deteriorates with more complex geometries. Also, the shadow region is dependent on the incident wave and we did no compression there, since it is not clear at this stage which modified visibility criterion would include the relevant stationary points on the illuminated side (as in Figure 2).

5.2 Adaptive asymptotic compression

Points that contribute to an oscillatory integral can be detected automatically using a sliding window $\xi(x-c)$ centered around a point c. If the window contains no contributing points, asymptotic theory (recall §2.1) predicts the windowed integral

$$F(c) = \int_a^b \xi(x-c) f(x) e^{ikg(x)} \mathrm{d}x$$

to be spectrally small in the frequency parameter k (for C^∞ integrands). Conversely, the function $F(c)$ can be expected to be large if the window around c does contain a contributing point.

In the context of integral equation methods, one can compute correlations between any two points on the boundary as integrals of the unmodified integrand times a moving window function. This can only be done a posteriori, since the integrand in (2) involves the density function which is unknown a priori. We compute correlations for each collocation point t_m, $m = 1, \ldots, N$, and use windows around center points σ_n, $n = 1, \ldots, 1.5N$. We use more centers than collocation points by a factor of 1.5 in order to determine more accurately where the important contributions are located. The window function we use around the center σ_n is

$$\xi(\tau - \sigma_n) = \chi(\tau - \sigma_n, -T, 0, 0, T),$$

with $T = 0.02$ in the examples below. We compute a correlation matrix R, with elements given by:

$$\begin{aligned} R_{m,n} &= \int_{\mathcal{K}} \xi(\tau - \sigma_n) K_{\mathcal{K}}(t_m, \tau) v_N(\tau) \mathrm{d}\tau \\ &= \sum_{j=1}^{N} c_j \int_{\mathcal{K}} \xi(\tau - \sigma_n) K_{\mathcal{K}}(t_m, \tau) \varphi_j(\tau) \mathrm{d}\tau \\ &\approx \sum_{j=1}^{N} \xi(t_j - \sigma_n) A_{m,j} c_j. \end{aligned} \tag{15}$$

Recall from (6) that $v_N(\tau)$ is our approximation to the density function. In the latter step, we have again approximated a windowed integral by a weighted sum of matrix elements of the dense discretization matrix A, which makes the computation of all correlations a very cheap operation. In the results of this section, we have used the integral formulation in (15).

For the compression phase, we retain all matrix elements corresponding to correlations higher than a fixed percentage ξ times the maximal correlation on each row. We devise a window that covers the retained centers, and smoothly decays to zero away. Care is taken in the implementation to merge windows that would otherwise overlap. The compressed matrix $\tilde{A}$ is computed in the same way as before, but this time using automatically computed window functions rather than a priori fixed windows. The percentages ξ that we used for the example obstacles in our experiments are indicated in Figure 14 with each obstacle.

Note that this procedure leads to a window for each collocation point at the wavenumber k_1 where the correlations are computed. At larger frequencies, the discretization may be refined and there may be more collocation points. For each of those points, we simply use the window of the closest collocation point at k_1.

An example of the correlation matrix is shown in the left panel of Figure 17, for the multiple scattering configuration with three ellipses (the ellipses are shown and numbered $1-2-3$ in Figure 14). Here, rows correspond to collocation points and columns to the centers. The sparsity pattern of the compressed discretization matrix is shown in the right panel. Both the correlation matrix and the discretization matrix have a 3×3 blocked structure, with each block corresponding to the coupling between two of the three ellipses. Asymptotic analysis of multiple scattering configurations shows that ultimately, rays bounce around in periodic orbits that mimize the distance between different obstacles [12, 1]. These periodic orbits appear as the vertical patterns in the coupling submatrices in Figure 17.

For example, consider the two blocks in the upper right of the computed correlation matrix. These two blocks correspond to collocation points on ellipse 1 or ellipse 2. The center point $\mathbf{p}$ that is indicated in Figure 17 (and in Figure 14) corresponds to the leftmost point on the third ellipse. The correlations are high when concentrated near $\mathbf{p}$, and this is physically the only region where rays can reflect off the third ellipse onto the other two along the shortest path, for a plane wave incidence from the left. Hence, that is where any of the stationary points must lie.

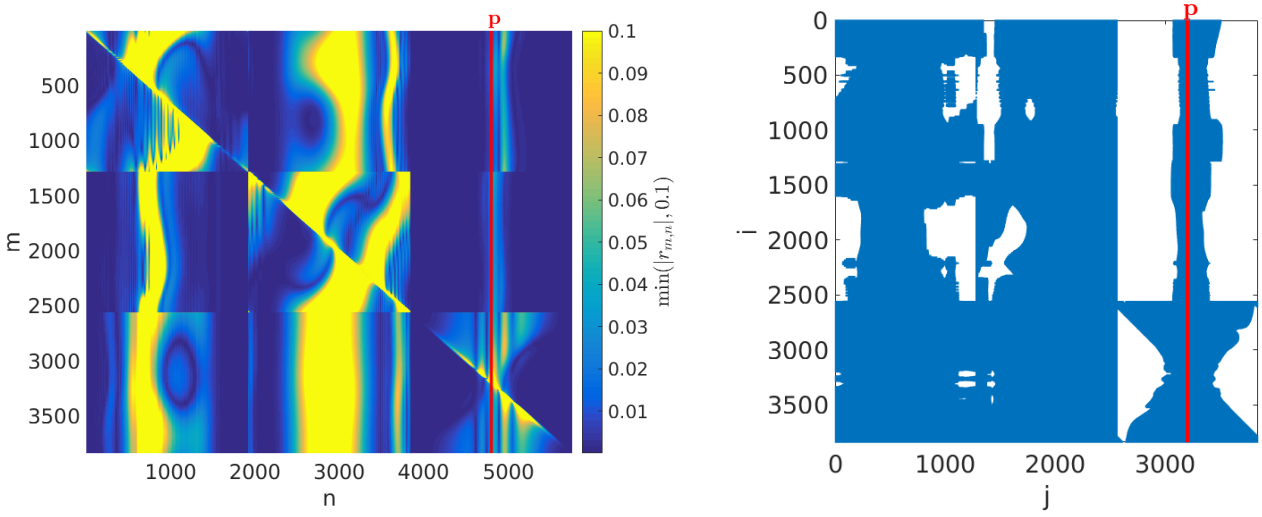

Figure 17: Correlation matrix $R_{m,n}$ at $k = 2^7$ (left) and nonzero pattern of $\tilde{A}$ (right) for the multiple scattering configuration with three ellipses.

Finally, the Green singularity is clearly visible in the correlation matrix along the diagonal. The diagonal blocks are the self-interaction of the ellipses, and they display a pattern much like the one we have seen before for a single circle in Figure 7. The diagonal blocks of the nonzero pattern of $\tilde{A}$ behave similarly, and this is more pronounced as the correlation threshold is increased.

The results are similar for all of the four non-inclusion single scattering obstacles. More specifically, a

collocation point in the shadow region has a stationary point in the illuminated region, in agreement with Remark 1. The computed correlations seem to follow the stationary points quite well.

For the near-inclusion obstacle, almost all of the illuminated region is included in the windows, due to the trapping of rays inside the cavity. As a result there is very little compression. Of course, one could not hope for much better in view of the complicated high-frequency behaviour of this obstacle. There is also a very high correlation near the points **q** and **s** indicated in Figure 14. An important side-effect is that some of the correlations near the diagonal, covering the Green function's singularity, were rather small. In the implementation we always include the Green singularity, regardless of the value of the correlations.

In the experiments in this section, the correlation matrix R was computed only at the lowest wavenumber. These correlations provide valuable high-frequency information as long as long as there is 'enough' high-frequency behaviour present at that value of k. Since the location of stationary points is essentially a geometrical feature, the stationary points are independent of frequency. Thus, we can use the windows at larger frequencies and achieve asymptotic compression, without a priori knowledge of the asymptotic behaviour of the solution.

k	128	256	512	1024
Error BC c	1.28e-2	1.08e-2	1.28e-2	1.50e-2
Error BC $\tilde{c}$	1.35e-2	1.09e-2	1.28e-2	1.50e-2

Table 3: Accuracy as a function of the wavenumber for the scattering configuration with two circular obstacles. The windows were computed using correlations at $k = 128$ and reused for larger wavenumbers. The errors indicate how well the scattered field matches the boundary condition, for the exact solution $c = A^{-1}b$ and the approximate solution $\tilde{c} = \tilde{A}^{-1}b$ computed after asymptotic compression.

The results for the multiple scattering configuration with two disks are shown in Table 3. The discretization error is around 1%. Using a threshold percentage of $\xi = 0.3\%$, we can compute the scattered field using the compressed matrix $\tilde{A}$ without additional loss of accuracy. The results are in closer agreement for larger k. The increasing accuracy at larger wavenumber is more pronounced in Table 4. There, we show the relative error of $\tilde{c} = \tilde{A}^{-1}b$ versus the exact solution $c = A^{-1}b$ for the polygonal domain. The error rapidly improves with increasing frequency.

k	128	256	512	1024
$\|\|c - \tilde{c}\|\|/\|\|c\|\|$	2.67e-1	3.28e-2	4.97e-3	3.60e-3

Table 4: The relative error on the solution vector $\tilde{c} = \tilde{A}^{-1}b$ after asymptotic compression, for scattering by the polygonal domain using windows fixed by the correlations $R_{m,n}$ computed at $k = 128$.

In the correlation approach thus far, the percentage of nonzero elements in the compressed matrix remains constant independent of the frequency. That is because we use fixed windows computed at the lowest wavenumber. The sparsity ranges between 38% for the (single) circle and 87% for the circle and near-inclusion obstacle.

Figure 18 shows that the percentage of nonzero elements decreases as the threshold percentage ξ is increased. The errors decrease with ξ until they reach the order of the error when using the full matrix A. This is shown in two ways: the error in satisfying the boundary conditions, and the error in the interior field. The total interior field should be zero for this particular Dirichlet problem. The error, averaged over 100 points in the disk taken randomly for each ξ, saturates at about 0.2% with and without compression. Note that the forward relative compression error $||\tilde{A}c - b||/||b||$ gives a good indication of the other errors. Hence, one can try asymptotically compressing a few rows of A with a high threshold ξ, and keep lowering it until the error in compressing a limited number of representative rows as in § 4.3 is low enough.

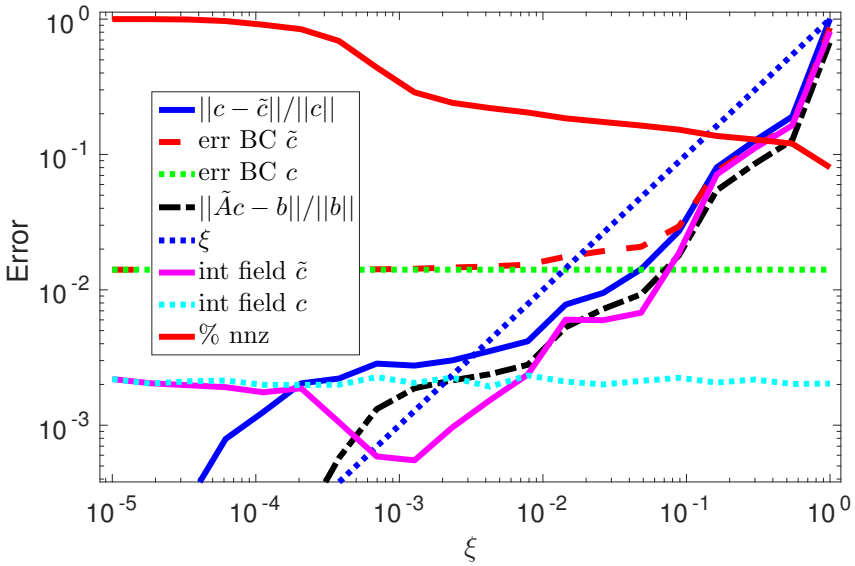

Figure 18: Errors as a function of the threshold percentage ξ at wavenumber $k = 2^{10}$ for the circular obstacle.

5.3 Adaptive recompression at higher frequencies

In the adaptive asymptotic compression technique thus far we have been using fixed windows computed at a small wavenumber. This leads to a fixed compression ratio, independent of the frequency. However, it should be possible to use smaller windows at larger frequencies, hence improving compression with increasing frequency. Recall that we achieved such gain in asymptotic complexity in §3.4 for the circular scatterer using precise knowledge of the stationary points. In the absence of prior asymptotic information, one way to achieve higher compression at higher frequencies in general is to recompute the correlations $R_{m,n}$ at each wavenumber.

Of course, computing the full correlation matrix is prohibitively expensive, since it requires the dense matrix A. However, if we have already computed a compressed matrix $\tilde{A}_1$ at a smaller frequency, then we can omit a large part of the computation. Indeed, if the correlation between two points on the boundary is small at a certain frequency, indicating that they are not asymptotically linked, it is safe to assume that their correlation will only be smaller at higher frequencies. Thus, we have to compute correlations only for the non-zero entries of $\tilde{A}_1$. Assuming some of these will be small, because the integrals are more oscillatory, this leads to a sparser matrix $\tilde{A}_2$ at a higher frequency. We can repeat this reasoning, where at each higher frequency we benefit from the improved sparsity of the previous stage.

To be precise, we introduce some notation. Say we have a range of strictly increasing wavenumbers k_j, $j = 1, \ldots, J$, and we use N_j degrees of freedom at each wavenumber k_j. In the full correlation technique, we would use $1.5N_j$ centers $\sigma_{j,n}$, $n = 1, \ldots, 1.5N_j$, for each collocation point $t_{j,m}$, $m = 1, \ldots, N_j$. This leads to $1.5N_j^2$ window functions $\xi(\tau - \sigma_{j,n})$ for each wavenumber k_j. The corresponding correlation matrix $R_{j,m,n}$ determines window functions $w_{j,m}$ to compute the compressed matrix $\tilde{A}_j$, and the solution of the discretized integral equation is $\tilde{c}_j = \tilde{A}_j \setminus b_j$.

We only compute the full correlation matrix R_1 at the smallest wavenumber k_1. For larger wavenumbers except the highest, after having computed the solution vector $\tilde{c}_j$ and the associated density function v_{N_j}, we only compute some of the elements of R_j:

$$R_{j,m,n} = \begin{cases} \int_{\mathcal{K}} \xi(\tau - \sigma_{j,n}) K_{\mathcal{K}}(t_{j,m}, \tau) v_{N_j}(\tau) \mathrm{d}\tau, & \text{if } \sigma_{j,n} \in \operatorname{supp} w_{j-1,m'}, \\ 0, & \text{otherwise.} \end{cases}$$

where m' is such that $t_{j-1,m'}$ is the closest collocation point to $t_{j,m}$. Subsequently, the element $R_{j,m,n}$ can be approximated by a weighted sum of elements of $\tilde{A}_j$ instead of A_j as before in (15), hence only requiring

sparse matrices at high frequencies. One can further reduce memory costs by not saving $R_{j,m,n}$ but only the resulting $\lambda_m, l_m, r_m, \rho_m$, although the former contains valuable information about the high-frequency behaviour and maybe even phase information. It would also be reasonable to decrease the support of the decaying part of the windows used for both $R_{j,m,n}$ and $\tilde{A}_j$, but we keep it fixed at 0.02 except for the Green singularity. Depending on the relative differences of consecutive wavenumbers k_j, the correlations $R_{m,n}$ do not have to be recomputed for a few j's. Finally, new windows are computed based on thresholding the correlations using a percentage ξ, and these are used for the compressed matrix $\tilde{A}_{j+1}$ at the next wavenumber.

First, we measure the efficiency of this frequency sweep with adaptive compression, compared to one where the full discretization matrix is constructed. We have used Matlab2015b on a 64-bit machine with 66 GB memory and 32 Intel(R) Xeon(R) CPU E5-2650 v2 CPU's at 2.6 Ghz: the results are shown in Table 5. At each wavenumber, it is faster to construct $\tilde{A}$ than the full matrix A, though the factor is not very large in this example. However, a large gain is observed when solving the resulting linear system using an iterative solver. Moreover, the gains accumulate in a frequency sweep. For this example, the total cost of constructing a full matrix at each of the listed wavenumbers and solving the associated linear system, is $6.86e3$ seconds (this is the sum of the first two rows of the table). In contrast, the total cost of computing all correlations, constructing all compressed matrices and solving the resulting linear systems, is $5.22e3$ seconds, or approximately three quarters of the cost of the full method. This gap is only expected to increase for larger wavenumbers: solving the linear system will become the dominant cost, which our method decreases through a sparse matrix and low number of iterations.

k	16	32	64	128	256	512	1024	2048
A	2.26e0	4.64e0	1.13e1	2.83e1	8.06e1	2.63e2	9.08e2	3.26e3
GM $A\backslash b$	1.26e-2	7.43e-2	2.47e-1	1.43e0	1.16e1	5.46e1	3.09e2	1.92e3
$R_{m,n}$	6.02e-1	8.10e-1	2.94e0	1.09e1	4.61e1	2.07e2	1.88e3	/
$\tilde{A}$	2.26e0	4.58e0	1.05e1	2.54e1	7.10e1	1.89e2	5.76e2	2.00e3
GM $\tilde{A}\backslash b$	1.21e-2	9.99e-2	2.49e-1	7.19e-1	3.08e0	7.99e0	3.08e1	1.41e2

Table 5: Time (s) for the different computations needed for the near-inclusion obstacle. We use linear basis functions and recompression in $\tilde{A}$.

Next, we measure the gain in compression for the different obstacles in Figure 19. The compression rate improves quite significantly with increasing wavenumber for all obstacles. For the single-scattering obstacles without cavity, the decay seems to be about $\mathcal{O}(k^{-1/2})$, like it was for the convex obstacle in §3.4. The amount of compression largely depends on the geometric properties of the scattering problem.

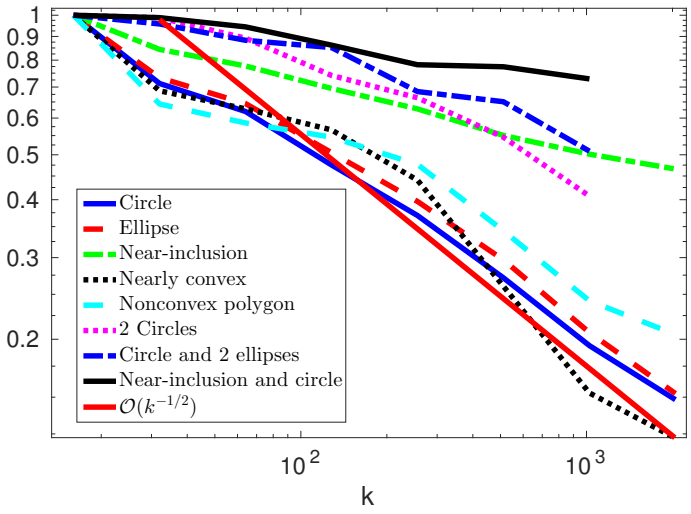

Figure 19: Fraction of nonzero elements in $\tilde{A}$ using adaptive recompression for increasing wavenumbers.

Table 6 shows that the errors of the method do not deteriorate when using adaptive recompression, even for an obstacle with complicated high-frequency behaviour.

k	16	32	64	128	256	512	1024	2048
Error BC $A\backslash b$	1.81e-2	1.65e-2	1.32e-2	1.39e-2	1.16e-2	1.62e-2	1.59e-2	1.87e-2
Error BC $\tilde{A}\backslash b$	1.81e-2	1.75e-2	1.42e-2	1.45e-2	1.19e-2	1.65e-2	1.61e-2	1.90e-2

Table 6: Average absolute or relative error on 100 boundary conditions for the near-inclusion obstacle using adaptive recompression.

Finally, Figure 20 shows that the improvement in condition number lowers the number of iterations of an iterative solver. We have used a non-restarted GMRES in Matlab with a tolerance of 10^{-5} for this experiment. The same qualitative behaviour is observed for all obstacles, using piecewise linear basis functions. The condition number improves by a factor of 1.1 to 3 compared to using fixed windows from correlations computed at $k = 2^7$, although the number of iterations varies less predictably about that range.

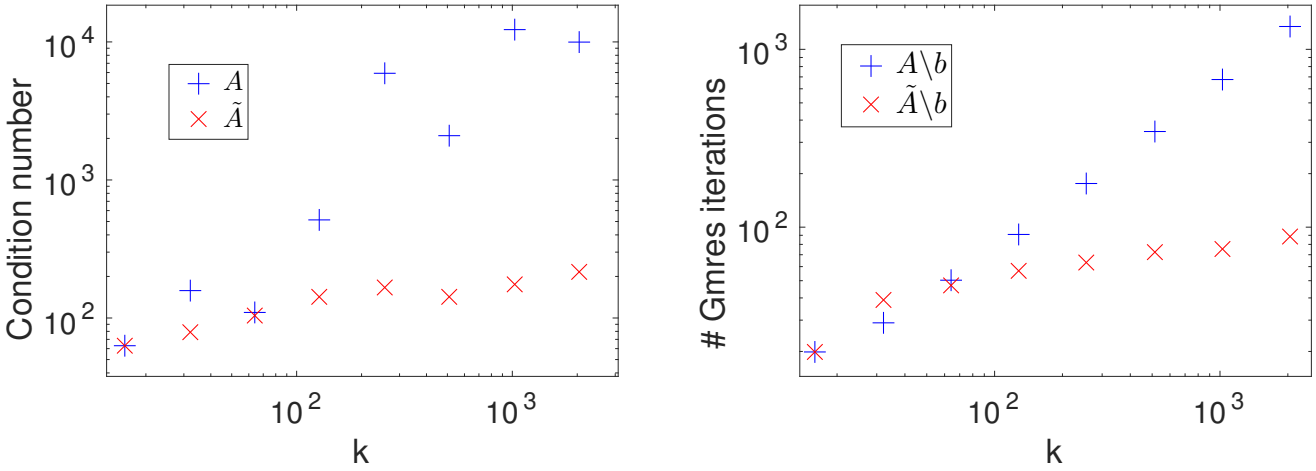

Figure 20: Condition number and number of GMRES iterations for the almost convex obstacle when using adaptive recompression.

6 Concluding remarks

Our results show that exploiting asymptotic behaviour in scattering problems is possible without a priori knowledge of the asymptotic behaviour of the solution. Compared to true asymptotic methods, our approach is very costly as all oscillations are still resolved with a fine discretization. Yet, the compression scheme applies to general objects and appears to be robust for problems with highly complicated high-frequency asymptotics.

There are several opportunities for further research. First, the present method may be combined with asymptotic methods. Ray tracing computations have been highly optimized in computer graphics, and fast algorithms making use of GPU acceleration include Kd-trees or Bounding Volume Hierarchies [25]. One can combine approximate asymptotic knowledge with the robustness of the present approach.

Alternatively, the method can be combined with non-asymptotic methods. The Fast Multipole Method yields a fast matrix vector product for discretizations of scattering problems, with optimal time and memory complexity. Since our method essentially amounts to modifying the Green's function, the two methods may be compatible. We also expect that sparsity can increase with k for an approximately fixed error in general 3D obstacles. This is the approach we intend to pursue for 3D scattering problems in the future.

We expect that this method also extends to penetrable objects like the ones studied in [17]: at least there, it is physically possible for stationary points to have a ray connecting them with a collocation point through a convex penetrable object, see Remark 1. In the case of stratified media as [4], we expect that stationary points will be shifted because of the modification in the Greens function.

Another way to gain compression and reduce complexity and condition numbers for general geometries is to refine the windows around the local maximum of the correlations. However, these local maxima of $r_{m,n}$ converge only slowly to the transition point in the case of a circle, because the bottom left of Figure 9 shows that there is a strong asymmetry. For a similar reason, counting the number of nearby zero crossings as a measure for oscillatoriness risks not including stationary points.

Note that the approach using correlations has some additional advantage. When determining the asymptotic expansion of the oscillatory integral as in [21], one computes the points where the gradient of the phase of the integrand is exactly zero and determines the contributions coming from them. This is implicitly done by the reflecting points in ray tracing. The correlations also find regions where the gradient of the phase is small (in absolute value) but does not cross zero. These regions have no contribution as $k \to \infty$, but a finite k might have to be very large for this contribution to become negligible. Thus, including these regions is also advantageous, which the correlation technique does.

Acknowledgments

The authors would like to thank Samuel Groth, Stephen Langdon, Niels Billen, Philip Dutré, Karl Meerbergen, Laurent Jacques, Alex Barnett, Yassine Boubendir and Dave Hewett for interesting and helpful discussions on this paper and related topics. The authors were supported by FWO Flanders [projects G.0617.10, G.0641.11 and G.A004.14].

References

[1] A. Anand, Y. Boubendir, F. Ecevit, and F. Reitich. Analysis of multiple scattering iterations for high-frequency scattering problems. II: The three-dimensional scalar case. *Numer. Math.*, 114:373–427, 2010.

[2] A. Asheim and D. Huybrechs. Extraction of uniformly accurate phase functions across smooth shadow boundaries in high frequency scattering problems. *SIAM J. Appl. Math.*, 74(2):454–476, 2014.

[3] V. M. Babich and V. S. Buldyrev. *Short-wavelength diffraction theory.* Springer-Verlag, Berlin, 1991. ISBN 978-3-642-83461-5.

[4] A. H. Barnett, B. J. Nelson, and J. M. Mahoney. High-order boundary integral equation solution of high frequency wave scattering from obstacles in an unbounded linearly stratified medium. *J. Comput. Phys.*, 297:407426, September 2015.

[5] N. Bleistein and R. A. Handelsman. *Asymptotic expansions of integrals.* Dover Publications, Inc., 31 East 2nd Street, Mineola, N.Y., 1986. ISBN 0-486-65082-0.

[6] O. Bruno, C. Geuzaine, J. J. Monro, and F. Reitich. Prescribed error tolerances within fixed computational times for scattering problems of arbitrarily high frequency: the convex case. *Phil. Trans. R. Soc. Lond. A*, 362:629–645, 2004.

[7] Chandler-Wilde, I. S., Graham, S. Langdon, and E. Spence. Numerical-asymptotic boundary integral methods in high-frequency acoustic scattering. *Acta Numer.*, pages 89–305, 2012.

[8] S. N. Chandler-Wilde, D. P. Hewett, S. Langdon, and A. Twigger. A high frequency boundary element method for scattering by a class of nonconvex obstacles. *Numerische Mathematik*, 129(4):647–689, 2015.

[9] H. Cheng, W. Y. Crutchfield, Z. Gimbutas, L. F. Greengard, J. F. Ethridge, J. Huang, V. Rokhlin, N. Yarvin, and J. Zhao. A wideband fast multipole method for the helmholtz equation in three dimensions. *J. Comput. Phys.*, 216(1):300 – 325, 2006.

[10] D. L. Colton and R. Kress. *Integral equation methods in scattering theory*. John Wiley & Sons, New York (N.Y.), 1983. ISBN 0-471-86420-X.

[11] V. Domínguez, I. G. Graham, and V. Smyshlyaev. A hybrid numerical-asymptotic boundary integral method for high-frequency acoustic scattering. *Numer. Math.*, 106:471–510, 2007.

[12] F. Ecevit and F. Reitich. Analysis of multiple scattering iterations for high-frequency scattering problems. I: The two-dimensional case. *Numer. Math.*, 114:271–354, 2009.

[13] C. Geuzaine, O. Bruno, and F. Reitich. On the O(1) solution of multiple-scattering problems. *IEEE Trans. Magn.*, 41(5):1488–1491, 2005.

[14] C. Geuzaine and J.-F. Remacle. Gmsh: a three-dimensional finite element mesh generator with built-in pre- and post-processing facilities. *International Journal for Numerical Methods in Engineering*, 79(11):1309–1331, 2009.

[15] E. Giladi. Asymptotically derived boundary elements for the Helmholtz equation in high frequencies. *J. Comput. Appl. Math.*, 198:52–74, 2007.

[16] L. Greengard and V. Rokhlin. A fast algorithm for particle simulations. *J. Comput. Phys.*, 73(2):325–348, 1987.

[17] S. P. Groth, D. P. Hewett, and S. Langdon. Hybrid numerical-asymptotic approximation for high-frequency scattering by penetrable convex polygons. *IMA J. Appl. Math.*, 80:324–353, 2015.

[18] R. F. Harrington. *Time-harmonic electromagnetic fields*. IEEE Press, 445 Hoes Lane, P.O. Box 1331, Piscatawat, NJ 08855-133 1, 1961. ISBN 0-471-20806-X.

[19] D. Huybrechs and S. Vandewalle. A sparse discretization for integral equation formulations of high frequency scattering problems. *SIAM J. Sci. Comput.*, 29(6):2305–2328, 2007.

[20] R. Kress and W. T. Spassov. On the condition number of boundary integral operators in acoustic and electromagnetic scattering. *Numer. Math.*, 42:77–95, 1983.

[21] R. B. Melrose and M. E. Taylor. Near peak Scattering and the corrected Kirchhoff Approximation for a Convex Obstacle. *Advances in Mathematics*, 55:242–315, 1985.

[22] P. Opsomer. https://github.com/popsomer/bempp.git, 2016. Release: Asymptotic compression version 1.

[23] V. Rokhlin. Rapid solution of integral equations of classic potential theory. *J. Comput. Phys.*, 60:187–207, 1985.

[24] W. Śmigaj, T. Betcke, S. Arridge, J. Phillips, and M. Schweiger. Solving Boundary Integral Problems with BEM++. *ACM T. Math. Software*, 41(2):6:1–6:40, 2015.

[25] I. Wald, W. R. Mark, J. Gunther, S. Boulos, I. Thiago, W. Hunt, S. G. Parker, and P. Shirley. State of the art in ray tracing animated scenes. *Eurograph.*, 2007.

[26] R. S. Wong. *Asymptotic approximations of integrals*. SIAM, 3600 Market Street, 6th floor, Philadelphia (Pa.) 19104-2688 USA, 2001. ISBN 978-0-898714-97-5, BKCL 0034, republication of 1944.

[27] T. Wu. *Boundary element acoustics*. WIT Press, 2000. ISBN 1-85312-570-9, reprint 2005.

[28] L. Ying. Fast directional computation of high frequency boundary integrals via local ffts. *SIAM Multiscale Model. Simul.*, 13(1):423–439, 2015.